



Parameterizing spectral surface reflectance relationships for the Dark Target aerosol algorithm applied to a geostationary imager

Mijin Kim^{1,2}, Robert C. Levy², Lorraine A. Remer³, Shana Mattoo^{2,4} and Pawan Gupta²

¹Goddard Earth Sciences Technology and Research (GESTAR) II, Morgan state university, Baltimore, MD 21251, USA

5 ²NASA Goddard Space Flight Center, Greenbelt, MD 20771, USA

³Goddard Earth Sciences Technology and Research (GESTAR) II, University of Maryland, Baltimore County, Baltimore, MD 21250, USA

⁴Science Systems and Applications (SSAI), Lanham, MD 20706, USA

Correspondence to: Mijin Kim (mijin.kim@nasa.gov)

10 **Abstract.** Originally developed for the Moderate Resolution Imaging Spectroradiometer (MODIS) in polar, sun-synchronous low-earth orbit (LEO), the Dark Target (DT) aerosol retrieval algorithm relies on the assumption of a Surface Reflectance Parameterization (SRP) over land surfaces. Specifically for vegetated and dark-soiled surfaces, values of surface reflectance in blue and red visible-wavelength bands are assumed to be nearly linearly related to each other and to the value in a shortwave infrared (SWIR) wavelength band. This SRP also includes dependencies on scattering angle and a normalized difference
15 vegetation index computed from two SWIR bands (NDVI_{SWIR}). As the DT retrieval algorithm is being ported to new sensors to continue and expand the aerosol data record, we assess whether the MODIS-assumed SRP can be used for these sensors. Here, we specifically assess SRP for the Advanced Baseline Imager (ABI) aboard, the Geostationary Operational Environmental Satellite (GOES)-16/East (ABIE). First, we find that using MODIS-based SRP leads to higher biases and artificial diurnal signatures in aerosol optical depth (AOD) retrievals from ABIE. The primary reason appears to be that
20 geostationary orbit (GEO) encounters an entirely different set of observation geometry than does LEO, primarily with regards to solar angles coupled with fixed view angles. Therefore, we have developed a new SRP for GEO that draws the angular shape of the surface bidirectional reflectance. We also introduce modifications to the parametrization of both red-SWIR and blue-red spectral relationships to include additional information. The revised Red-SWIR SRP includes solar zenith angle, NDVI_{SWIR}, and land-type percentage from an ancillary database. The blue-red SRP adds dependencies on the scattering angle
25 and NDVI_{SWIR}. The new SRPs improve the AOD retrieval of ABIE in terms of overall less bias and mitigation of the overestimation around local noon. The average bias of DT AOD compared to AERONET AOD shows a reduction from 0.082 to 0.025, while the bias of local solar noon decreases from 0.118 to 0.029.

1. Introduction

30 Aerosols in the atmosphere strongly influence the Earth's energy budget by absorbing and scattering solar radiation, and by acting as cloud condensation nuclei and ice nuclei to alter cloud micro- and macrophysics (Boucher et al., 2014). They also



play an important role in global atmospheric chemistry and the biogeochemical cycle (Kanakidou et al., 2018), and affect local air quality as particulate matter. Satellite remote sensing is beneficial to monitor atmospheric aerosol on the global scale. Broad coverage allows capturing widespread distribution and long-range transport of aerosol (Yu et al., 2013), and can help determine aerosol effects on climate and air quality.

35 Taking advantage of satellite observations, numerous efforts have been made to infer global distributions of aerosol optical properties. The procedure to infer aerosol loading and characteristics over ocean takes advantage of the relatively well-known surface reflectance properties of the ocean surface. Land surface variability makes it much more difficult to do the same over land with its hard to predict dynamic surface reflectance. Over 25 years ago, Kaufman and Remer (1994) and Kaufman et al. (1997b) noted that for vegetation and dark-soiled surfaces, the land surface reflectance in some visible (VIS) wavelengths

40 were highly correlated with each other, and also with values measured in some shortwave infrared (SWIR) wavelengths. This led to an aerosol retrieval approach over land used for MODIS (e.g., Kaufman et al., 1997a), for which after modifications is known as the ‘Dark Target (DT) aerosol algorithm’ (Remer et al., 2008, 2005; Levy et al., 2013, 2007a, b, 2010, 2013). In the original version (Kaufman et al., 1997a), the surface reflectance parameterization (SRP) assumed that the values in the 0.47 μm blue and the 0.65 μm red bands were set to be $\frac{1}{4}$ and $\frac{1}{2}$ the values in the 2.11 μm SWIR band. With the current

45 MODIS version, instead of simple ratios, the spectral relationship includes the slopes and intercepts of their regressions. In addition, the current SRP includes dependencies on scene identification. It was noted during the first years of MODIS on-orbit data collection that bidirectional reflectance introduced angular dependencies in the SRPs, and these dependencies were parameterized in subsequent algorithm versions as a function of scattering angle (Levy et al., 2007b; Remer et al., 2001). This DT retrieval algorithm has led to derivation of a 20+ yearlong AOD record that has an outstanding performance and relied on

50 by an extensive user community. Highly accurate aerosol products of the DT algorithm have not only contributed to improving theoretical understanding about the role of aerosols in radiation and climate (e.g., Boucher et al., 2014), but they have also been used for monitoring surface air quality (e.g., Al-Saadi et al., 2005; Chu et al., 2003) and a variety of other applications (Remer et al., 2020).

In order to continue the aerosol data record after the decommissioning of the MODIS missions on both Terra and Aqua, the

55 DT algorithm is being ported to other sensors. For example, Sawyer et al., (2020) discuss porting DT to the Visible-infrared Radiometer Suite (VIIRS) which is also on polar-orbiting satellites in Low Earth Orbit (LEO). Yet, as geostationary orbit (GEO) sensors now include the capability to measure both visible and SWIR reflectance, the DT algorithm can also be adapted to advanced imagers in GEO, such as the Advanced Himawari Imager (AHI) on board the Japanese HIMAWARI-8 satellite and the Advanced Baseline Imager (ABI) on board National Oceanic and Atmospheric Administration’s (NOAA) operational

60 Geostationary Operational Environmental Satellite (GOES) series. Continuous imaging by GEO satellites is valuable to capture diurnal variations of aerosol occurring with human activity cycles, outbreak of emission episodes, and long-range transport (Kim et al., 2020).

Although the new advanced imagers observe a similar spectral range (visible through thermal infrared) as MODIS, there are generally fewer bands in total, and the wavelength range of analogous bands are shifted. Levy et al. (2015) and Sawyer et al.



65 (2020) showed that with minimal change to SRP and slight adjustments for wavelength band, one could derive a VIIRS AOD product that had error/bias statistics similar to the MODIS product. Presumably, only small changes were necessary because VIIRS offers similar observing geometry to MODIS (i.e., both MODIS and VIIRS pass over the equator ± 1.5 hours around noon).

However, because there are much larger differences in ground sampling and viewing geometry between LEO and GEO, the
70 SRPs optimized for MODIS or similar LEO sensors do not appear to be appropriate for GEO. For example, Gupta et al. (2019) finds biases in a similar DT-algorithm applied to AHI on Himawari-8. Also, when analyzing NOAA's aerosol products created from ABI in the GOES-East position (e.g. ABIE), Zhang et al. (2020) showed the need for an empirical correction to improve mean bias and Root Mean Squared Error (RMSE).

The DT algorithm is also being ported to ABI and will be used to test a GEO-LEO synergy concept
75 (<https://www.earthdata.nasa.gov/esds/competitive-programs/measures/leo-geo-synergy>). This initial (baseline) version of ABI's DT-algorithm accounts for shifted wavelengths in calculating aerosol/Raleigh lookup tables and cloud masking. However, this baseline version assumes the values of the MODIS SRP, with no modifications for the GEO's very different observation of Earth's surface (regional versus global), and geometry (each site from a fixed sensor view, but widely varying solar angles).

80 Therefore, assuming that biases in retrievals may be due, at least in part, to GEO's sampling, we use strategies laid out by Levy et al. (2007b), and focus on GOES -16 ABI (ABI East, ABIE). We derive the atmospherically corrected spectral reflectance (AC-ref) and investigate its angular variation and the variation of land cover type. The result is a new SRP, and we test this new SRP on ABI data and compare the aerosol results with the baseline (assumed MODIS SRP).

This manuscript is organized as follows. Section 2 introduces the original DT algorithm for MODIS and a baseline for GEO
85 sensors. Section 3 compares GEO ABI and LEO MODIS observations from perspective of geometric differences and identifies an issue in the baseline AOD retrieval from GEO. Methodologies and input datasets for the atmospheric correction calculation are described in Sect. 4, and an investigation of new SRP is conducted in Sect. 5. Section 6 presents the performance of the new SRP and compares the newly retrieved GEO AOD with AOD from Aerosol Robotic Network (AERONET). A discussion and conclusion are presented in Sect. 7 and Sect. 8, respectively.

90 2. Data and Methodology

2.1 MODIS Dark Target aerosol retrieval algorithm and products

MODIS, aboard the Terra and Aqua sun-synchronous polar-orbiting satellites, measures radiance of Earth-viewing scenes in
36 spectral bands spanning the deep blue at $0.41 \mu\text{m}$ to thermal infrared (TIR) at $14 \mu\text{m}$. Each MODIS obtains near-global coverage twice a day, once during daytime and once at night at nominal spatial resolutions of 0.25 to 1.0 km, providing
95 geolocated, calibrated spectral radiances known as the Level 1B data. The MODIS DT aerosol algorithm uses subsets of the



spectral bands and follows separate logic to derive aerosol properties over land and the ocean. Although both land and ocean retrievals are based on a Look Up Table (LUT) inversion approach, each uses its own set of assumptions for estimating surface reflectance (SR) and aerosol optical models. This study focuses on the over-land part of the DT algorithm, specifically the assumptions of the SRP. Details of the DT land algorithm are well described online (<https://darktarget.gsfc.nasa.gov/>) and previous DT algorithm studies (Levy et al., 2007b, 2010, 2013; Gupta et al., 2016; Remer et al., 2005), but we summarize here.

Radiance from the sun is absorbed and reflected by constituents of the atmosphere and the surface. The satellite observes some of that signal at the theoretical top-of-atmosphere (TOA). To retrieve the aerosol characteristics, the signal from the atmosphere must be separated from the signal originating from the land surface beneath. The unique aspect of the DT algorithm lies in how the algorithm assumes the surface reflectance to make that separation – and the assumptions about the surface are known as the SRP.

Vermote et al. (1997) describe the process of atmospheric correction (AC), which essentially “subtracts” the constituents of the atmosphere from the TOA signal, given the knowledge of atmospheric properties such as molecular scattering and aerosol properties. Prior to launch of Terra, Kaufman et al. (1997a) performed AC using proxy MODIS measurements from existing satellite and low-flying aircraft. They showed there were near-linear relationships of SR values in the blue, red and SWIR wavelength bands over natural surfaces such as vegetation and dark soils. Specifically, they found that the value of surface reflectance in the blue (e.g. 0.47 μm) and red (0.65 μm) wavelengths were approximately $\frac{1}{4}$ and $\frac{1}{2}$ of the surface reflectance in the SWIR (2.11 μm), respectively, and that these ratios were invariant of solar/sensor/scattering geometry. Physically, this relationship was expected based on the relative balance between absorption of visible radiation by chlorophyll versus absorption of SWIR radiation by the water within the vegetation.

Kaufman et al. (1997b) realized that these observed relationships defined an SRP, to be used as a constraint during the aerosol retrieval. Since aerosol (especially fine-sized particles indicative of anthropogenic or burning processes) is often nearly transparent at 2.11 μm , MODIS essentially observes the 2.11 μm surface reflectance. That initial estimate of 2.11 μm surface reflectance leads to an easy estimate of the 0.47 and 0.65 μm surface reflectance. As a result, the aerosol contribution (and derivation of aerosol optical depth) is related to the difference between the estimated surface and the observed TOA reflectance at 0.47 and 0.65 μm . This SRP (blue = $\frac{1}{4}$ of SWIR, red = $\frac{1}{2}$ of SWIR), was coded into the at-launch MODIS algorithm (Kaufman et al., 1997a; Remer et al., 2005).

Although the initial MODIS aerosol product compared well to sunphotometer (Chu et al., 2002; Remer et al., 2005), Levy et al. (2005) found some systematic biases that suggested revisiting SRP. By then, there were more ground-based sunphotometers and multiple years of MODIS observations, so that global AC was expected to yield new information. The result was when regressing blue, red, and SWIR values, best-fit slopes were different from the original ratios, and there were non-zero y-offsets. Furthermore, variability of the blue/red and red/SWIR y-offsets and slopes appeared to depend on observing geometry and surface type (Levy et al., 2007b). As a result, the current version of the MODIS-DT algorithm includes SRPs which also



depend on scattering angle (Θ) and surface “greenness” in the form of a Normalized Difference Vegetation Index based on
 130 two SWIR channels (2.11 μm and 1.24 μm)

$$NDVI_{SWIR} = (\rho_{1.24}^m - \rho_{2.11}^m) / (\rho_{1.24}^m + \rho_{2.11}^m), \quad (1)$$

where $\rho_{1.24}^m$ and $\rho_{2.11}^m$ are the measured top-of-atmosphere reflectances in the 1.24 μm and 2.11 μm wavelengths, respectively.

The current version of the algorithm (e.g., MODIS Collection 6.1) uses SRPs as follows:

$$\rho_{Red}^s = \rho_{SWIR}^s \times slope_{RedSWIR} + yint_{RedSWIR},$$

$$135 \quad \rho_{Blue}^s = \rho_{Red}^s \times slope_{BlueRed} + yint_{BlueRed}, \quad (2)$$

where,

$$slope_{RedSWIR} = slope_{RedSWIR}^{NDVI_{SWIR}} + 0.002\theta - 0.27,$$

$$yint_{RedSWIR} = -0.00025\theta + 0.033, slope_{BlueRed} = 0.49,$$

$$and \ yint_{BlueRed} = 0.005, \quad (3)$$

140 where in turn

$$slope_{RedSWIR}^{NDVI_{SWIR}} = 0.58, NDVI_{SWIR} < 0.25,$$

$$slope_{RedSWIR}^{NDVI_{SWIR}} = 0.48, NDVI_{SWIR} > 0.75,$$

$$slope_{RedSWIR}^{NDVI_{SWIR}} = 0.58 - 0.2(NDVI_{SWIR} - 0.25), 0.25 \leq NDVI_{SWIR} \leq 0.75. \quad (4)$$

The scattering angle (Θ) is defined as

$$145 \quad \theta = \cos^{-1}(-\cos\theta_0\cos\theta + \sin\theta_0\sin\theta\cos\varphi), \quad (5)$$

where θ_0 , θ , and φ are the solar zenith angle (SZA), viewing zenith angle (VZA), and relative azimuth angles (difference between solar and sensor azimuth angles, RAA), respectively.

For Collection 6.1 of the MODIS product, Gupta et al., (2016) added a correction to the $slope_{RedSWIR}^{NDVI_{SWIR}}$ and $yint_{RedSWIR}^{NDVI_{SWIR}}$ to account for an urban surface. The urban correction takes into account the pixels with urban percentage (UP) larger than 20%

150 as follows:

Where $NDVI_{SWIR} < 0.20$

$$slope_{RedSWIR}^{NDVI_{SWIR}} = 0.78 \text{ and } yint_{RedSWIR}^{NDVI_{SWIR}} = -0.02, 20\% \leq UP < 50\%,$$

$$slope_{RedSWIR}^{NDVI_{SWIR}} = 0.66 \text{ and } yint_{RedSWIR}^{NDVI_{SWIR}} = 0.02, UP \geq 50\%, \quad (6)$$

and where $NDVI_{SWIR} \geq 0.20$

$$155 \quad slope_{RedSWIR}^{NDVI_{SWIR}} = 0.62 \text{ and } yint_{RedSWIR}^{NDVI_{SWIR}} = 0.0, 20\% \leq UP < 70\%,$$

$$slope_{RedSWIR}^{NDVI_{SWIR}} = 0.65 \text{ and } yint_{RedSWIR}^{NDVI_{SWIR}} = 0.0, UP \geq 70\%. \quad (7)$$

The Urban Percentage is defined as the percentage of pixels (500m) identified as urban land cover type, MCD12Q1). The dataset of land cover type will be introduced in Sect. 2.4.

This SRP is used as a constraint within the DT retrieval algorithm. The rest of the retrieval algorithm can be summarized by

160 the following steps A-C:



- 165 A. Prior to any retrieval, there exists a set of pre-computed aerosol/atmospheric properties known as LUTs. These LUTs are derived using radiative transfer (RT) code (Evans and Stephens, 1991) and represent the atmospheric portion (aerosol plus molecular) of the TOA signal. Spectral TOA reflectances are computed for different loadings of each of these aerosol “types” (or models) (indexed by AOD at $0.55 \mu\text{m}$), and combinations of solar and satellite zenith (θ_0 and θ) and relative azimuth angles (ϕ). There are five distinct aerosol types represented based on assumed size distributions, shape characteristics, and spectral complex refractive indices. Vertical profiles for aerosols compared to molecular/Rayleigh scattering is also assumed. Details on aerosol model assumptions for LUT calculation and DT retrieval process are in Levy et al. (2007a) and Levy et al. (2013). For MODIS, LUTs are calculated for the green (e.g., $0.55 \mu\text{m}$) in addition to the blue, red, and SWIR bands.
- 170 B. Using the observed L1B spectral reflectance and radiance data, the DT algorithm takes several steps for pre-processing and data aggregation. These steps include aggregating into $N \times N$ boxes of native pixels (e.g., 20×20 boxes of 0.5 km native pixels to make $10 \text{ km} \times 10 \text{ km}$), masking (removing) pixels that appear to be clouds, in-land water bodies, and snow/ice, correcting for trace-gas absorptions (Patadia et al., 2018), and calculating statistics (mean, standard deviation) of the corrected, non-masked pixels in the box. We denote this cleaned reflectance as the ‘Mean_Reflectance_Land’.
- 175 C. Based on ground-based climatology, one of the three choices for fine-dominated model (“weakly-absorbing fine-dominated”, “moderately-absorbing fine-dominated”, “strongly-absorbing fine-dominated”) is prescribed by location and season, with the chosen value being known as ‘Aerosol_Type_Land’.-The algorithm subsets the LUT, pulling out the portion representing the observed geometry for the prescribed Aerosol_Type_Land and the “dust-like coarse-dominated” models. Armed with the SRP of Eq. (1-5), the retrieval attempts to search this subsetted LUT for a linear combination of the prescribed aerosol types that best matches the Mean_Reflectance_Land vector. The solution leads to a derivation of the total aerosol AOD (at $0.55 \mu\text{m}$), the spectral AOD (in the blue, red, and SWIR bands), and a weighting of the non-dust model to the total known as the ‘Fine_Model_Fraction’ (FMF). A by-product (diagnostic) of this process is the spectral surface reflectance meeting the SRP known as the ‘Surface_Reflectance_Land’.
- 180
- 185

The collection of derived aerosol properties and diagnostic variables is contained within the archived MODIS “Level 2” (L2) product known as MOD04 for MODIS on Terra and MYD04 for MODIS on Aqua the values of the variables calculated in Steps A-C are written to the file. Here, we are interested in the vectors of the TOA Mean_Reflectance_Land (plotted as “MODIS Level 2 TOA reflectance”), derived spectral AOD (reported as ‘Corrected_Optical_Depth_Land’) and fine model fraction (‘Optical_Depth_Ratio_Small_Land’), as well as the diagnostic Surface_Reflectance_Land.

190

The current assumptions for MODIS_SRP were derived by performing AC of the Mean_Reflectance_Land vector over globally distributed AERONET sites. Even though we confirmed the basic SRP for use in Collection 6.1 (e.g., Levy et al., 2013), there have been both increases in AERONET coverage as well as a much larger dataset of Mean_Reflectance_Land.



195 Yet, the ABIs are *regional* in coverage, which means that only a subset of global AERONET sites can be observed by any
single ABI. Therefore, to compare with the ABI datasets described in the next section, we perform AC on the subset of the
AERONET sites that are observed by the corresponding ABI. We also constrain this analysis to the MODIS data between
2015-2019, which better matches the AERONET coverage observed by each ABI during 2019. Single wavelength outputs
from this exercise are known as AC-ref, which will be regressed to derive the SRP. Section 2.3 introduces AERONET data
200 and a description of its collocation with ABI observations.

2.2 ABI and Baseline Dark Target aerosol retrieval algorithm

The ABI is a multi-band sensor aboard the GOES-R series of geostationary satellites. The GOES-R series currently in-orbit
include GOES-16 (launched as GOES-R in November 2016) operating at the GOES-East position at 75° West longitude,
GOES-17 (launched as GOES-S in March 2018) operating at the GOES-West position at 137° West, and GOES-18 (launched
205 as GOES-T in March 2022) in testing mode. Each ABI has 16 channels, ranging from the blue (0.47 μm) to thermal infrared
(13.3 μm). The red channel (0.64 μm) is observed at spatial resolution of 0.5 km (subsattellite point), with blue (0.47 μm),
Near Infrared (NIR; 0.86 μm), and SWIR (1.60 μm) bands at 1 km, with the remainder (1.37 μm , 2.26 μm , TIR bands) at 2
km. Note there is neither a green (~ 0.55 μm) nor 1.24 μm SWIR band as MODIS. Finally, since 2019, all ABIs observe using
a scanning pattern that results in “Full Disk” (FD) images every 10 minutes. As all ABIs include blue, red, and SWIR channels
210 (0.47 μm , 0.63 μm and 2.24 μm) similar to MODIS, our initial assumption is that the MODIS SRP can be used for both ABIE
(on GOES-East) and ABI-W (on GOES-West).

With that in mind, we are following the Gupta et al. (2019) approach for AHI and applying to ABI. The initial or “baseline”
version of the DT aerosol algorithm on ABI generally follows the same logic as that on MODIS (steps A-C in Sect. 2.1). the
DT algorithm for ABI has key differences from that used for MODIS, including:

- 215 1) Aerosol/Rayleigh LUTs and gas corrections are pre-calculated for the ABI-specific wavelength bands, and aerosol
types are assumed to have spectral refractive index with the same values as analogous wavelengths on MODIS (e.g.,
ABI \rightarrow MODIS wavelengths: 0.47 \rightarrow 0.47, 0.64 \rightarrow 0.65, 2.26 \rightarrow 2.11 μm).
- 220 2) Different from MODIS is in creating $N \times N$ boxes of native pixels. ABI has one higher-resolution band (e.g., 0.5 km
for the red 0.63 μm band), three middle-resolution bands (1.0 km for the blue 0.47 μm , NIR 0.87 μm , and SWIR 1.61
 μm bands), and 12 lower resolution bands (2.0 km). The red band is used for high resolution cloud masking; the other
ABI bands are aggregated by 10 x 10 pixels at 1 km to create a 10 km box, unlike the MODIS algorithm, which uses
20 x 20 pixels at 0.5 km to create the 10 km.
- 225 3) The $\text{NDVI}_{\text{SWIR}}$ test uses 0.86 μm rather than 1.24 μm for comparison with 2.26 μm due to the lack of a 1.24 μm
channel and the shift of the “2 μm channel” (from 2.12 to 2.24 μm). While not as “aerosol-free”, vegetation reflects
0.86 μm similar to 1.24 μm (Miura et al., 1998). Let us denote $\text{NDVI}_{\text{LEO_SWIR}}$ as $\text{NDVI}_{\text{SWIR}}$ defined in Eq. (1), and
define $\text{NDVI}_{\text{GEO_SWIR}}$ as;



$$NDVI_{GEO_SWIR} = (\rho_{0.87}^m - \rho_{2.24}^m) / (\rho_{0.87}^m + \rho_{2.24}^m) \quad (8)$$

For convenience, it is commonly named $NDVI_{SWIR}$ regardless of the difference in wavelength hereafter.

- 4) Cloud and ice/snow masking are modified to account for lack of 1.24 μm and some of the TIR bands.
- 5) Note that the retrieval does not require a green band reflectance as input, although like MODIS, it reports “indexed” AOD at 0.55 μm .

We apply this baseline GEO DT algorithm to ABI observations to derive Level 2 FD aerosol products at 10 km \times 10 km nominal resolution, which therefore includes its own “Mean_Reflectance_Land” vector (of TOA cloud-cleared, gas-corrected reflectances). Nominally, ABI produces six full disk images every hour in default FD scan mode. However, to reduce data volume, we work here with one image each hour and limit to FD data collected between July 2019 to June 2020. For ABI, one year is sufficient to produce the necessary statistics because of ABI’s higher temporal resolution. Again, note that while the baseline DT-ABI algorithm uses the SRP defined by MODIS, AC of the Mean_Reflectance_Land is expected to lead to an improved definition of SRP for ABI.

2.3 AERONET AOD and collocation criteria

The globally distributed AERONET network has provided aerosol optical properties for \sim 30 years (Giles et al., 2019), and has increased to nearly 540 sites worldwide. The AERONET AOD dataset is widely used as ground truth for satellite retrievals because of its well-defined accuracy and instrument quality control. The uncertainty of an AOD measurement from a newly calibrated field instrument under cloud-free conditions is less than ± 0.01 for wavelengths longer than 0.44 μm (Giles et al., 2019; Eck et al., 1999). Here, we utilize the Level 2.0 all-point, sun-observed AODs provided by the AERONET Version 3 algorithm and interpolate AERONET-provided spectral AODs to AOD at 0.55 μm using a quadratic fit in log-log space (Eck et al., 1999). The AERONET AOD at 0.55 μm is then used for two different purposes.

- 1) The AERONET AODs are used to generate an AC-ref from MODIS and ABIE observations. In this case, data are adopted where AOD at 0.55 μm is less than 0.2 and Ångström exponent (AE) (0.44 – 0.675 μm) is greater than
- 2) The AERONET AODs are also used to validate the DT-derived AOD.

The 193 AERONET site are used in this study. Spatiotemporal criteria for the satellite-AERONET co-locations are as follows. For AC-ref calculation, AERONET observations within ± 15 minutes of satellite overpass (MODIS or ABIE) are collocated with satellite-derived TOA reflectance within $\pm 0.3^\circ$ rectangular grid centered over an AERONET site. For the purpose of AOD validation, a temporal criterion of ± 15 minutes for AERONET AOD and a spatial criterion of $\pm 0.2^\circ$ for DT AOD are applied.



2.4 Land cover type

260 MODIS Land Cover Type (MCD12Q1) version 6 products provide global land cover types from the Terra and Aqua combined
measurement at yearly interval with 500 m sinusoidal grid resolution (<https://lpdaac.usgs.gov/products/mcd12q1v006/>). There
are Land cover indices classified from six different classification scheme. In this study, International Geosphere-Biosphere
Programme (IGBP)'s classification (Belward et al., 1999; Sulla-Menashe and Friedl, 2018) is applied to investigate the
changes in spectral relationship owing to land cover type. The IGBP's index classified 16 land cover types include Forests
(index 1-5), Shrublands (index 6-7), Savannas (index 8-9), Grasslands (index 10), Permanent Wetlands (index 11), Croplands
265 (index 12), Urban and Built-up lands (index 13), Cropland/Natural vegetation mosaics (index 14), Permanent Snow and ice
(index 15), Barren (index 16), and Water bodies (index 17).

We first assign the percentage land type [%land type, hereafter] to the AC-ref derived at each AERONET site, using the same
0.3° distance around the AERONET station as done to calculate AC-ref. For the retrieval processing, 0.1° x 0.1° gridded map
of land cover type is derived. Detailed collocation process is explained in Sect. 5.2.1 and Sect. 6.1.

270 3. Analysis of baseline DT-ABI algorithm

3.1 Differences in viewing geometries

MODIS (and its follow-on VIIRS sensors) provide global aerosol coverage, but by observing a given ground target at
approximately the same time every day. To observe more rapid aerosol changes, as well as to characterize the aerosol diurnal
cycle, we use imagers on GEO satellites. However, there are great differences between the observing geometry of ABI and
275 MODIS. In a sun-synchronous polar-orbiting orbit, MODIS views a given ground target from a wide variety of VZA and RAA
over a period of several weeks, while SZA varies slowly. In contrast, ABI views each Earth scene from a constant VZA, while
the sun moves from sunrise to sunset introducing a variable SZA. Figure 1(a) maps the VZA of ABIE, which is constant for
all FD images. On the other hand, Fig. 1(b) and (c), show that the MODIS VZA varies, even on consecutive days. For example,
when observing the GSFC AERONET site (red circle in Fig. 1), the VZA of ABIE is fixed at 45.42°, whereas the VZA of
280 MODIS changes from 15.88° to 51.11°.

Figure 2 shows frequency distributions of scattering angle, SZA, VZA, and RAA of ABIE and MODIS observation at the
GSFC AERONET site (-76.84°E, 38.99°N). In general, ABIE measures various solar angles as it provides multiple images
for a location throughout a day. Figure 2a shows the SZA varying from 10° (noon during the summer solstice) to 90°
(sunrise/sunsets all year), with the most frequent observations having SZA in the range of 60°-70°. With the sun moving from
285 horizon to horizon during the day, the RAAs vary from 60° to 180° with the median value of 125.8° (Fig. 2c). This is from
VZA fixed at 45.42° (Fig. 2e). Thus, under the fixed VZA condition, scattering angle of ABIE measurement changes in
accordance with the variations of solar angles.



Compared to ABIE, MODIS measures limited solar angles because it flies in a sun-synchronous polar orbit. As both Terra or Aqua observe GSF C approximately ± 1.5 hours from local solar noon, neither MODIS observes sunrise or sunset ($SZA = 90^\circ$). Thus Fig. 2(b) shows that MODIS SZA is never higher than 70° and is most commonly in the range of $20\text{--}30^\circ$, unlike ABIE SZA, which was peaked in the range of $60^\circ\text{--}70^\circ$. The RAAs showed a bimodal distribution that peaked at 50° and 130° (Fig. 2d) and was absent in the range between 60° and 120° . Meanwhile, MODIS measures at various VZA conditions in the range of 0° to 60° . Accordingly, the scattering angle of MODIS is synchronized with the VZA variation rather than the limited solar angle variability. Although both scattering angle distribution in Fig. 2(g) and Fig. 2(h) cover the same angular range, the main factor determining the variation is not the same.

3.2 Bias in current ABI AOD and why we suspect surface reflectance.

We apply the baseline DT-ABI algorithm to ABI observations on GOES-16 (ABIE) and GOES-17 (ABI-West, ABIW) from August to September 2019 on an hour-by-hour basis. Figure 3 displays average bias in the retrieved AOD versus AERONET AOD in each hour with standard deviation. Most obvious is that the DT AODs retrieved from both ABIE (Fig. 3a) and ABIW (Fig. 3b) show a time dependent bias variation and have a peak in the error at local noon or early afternoon.

We hypothesize that the diurnal signature in bias between each ABI and AERONET arises because the viewing geometry of the GEO sensor has different features than from the LEO one (Fig. 2). We must remember that for GEO sensors, a particular ground site is always observed with the same viewing angle while the sun angles change throughout the day. ABI observes each ground pixel with a fixed VZA, and therefore each VZA matches up to a specific land cover type according to location. In contrast, since MODIS has a 16-day orbit repeat cycle (<https://ladsweb.modaps.eosdis.nasa.gov/missions-and-measurements/modis/>), a particular ground target will be observed from a variety of viewing zenith angles, while the solar zenith angle is relatively constant during a season. Thus, any residual bias escaping the LEO SRP's compensation for anisotropic surface reflectance by assuming a dependency on scattering angle will be averaged out over MODIS's 16-day repeat cycle but be reinforced day after day with ABI. From this point of view, we suspect that while assuming that the scattering angle represents the anisotropic reflectance pattern may work for MODIS on average, it would induce a large bias to GEO retrievals at local noon and/or dawn and dusk. This means we should consider a new SRP for ABI observations that covers the new geometry. We will proceed with creating this new SRP and then show that it reduces biases and mitigates the bias's diurnal signature in retrieved AOD.



4. Atmospheric correction

315 4.1 Calculating Atmospherically-Corrected reflectance (AC-ref)

To develop a new SRP, we require a data set of spectral surface reflectance. To a first approximation, the wavelength-dependent reflectance measured by a sensor at the TOA reflectance ρ_λ^* is the sum of contributions by the atmosphere-only (known as the path reflectance) and the surface-atmosphere interaction (Kaufman et al., 1997a).

$$\rho_\lambda^* = \rho_\lambda^a + \frac{F_{d\lambda} T_\lambda \rho_\lambda^s}{(1 - s_\lambda \rho_\lambda^s)} \quad (9)$$

320 Here, the first term ρ_λ^a is atmospheric path reflectance which consists of molecular and aerosol extinction, and the second term represent interaction of atmosphere and underlying surface. $F_{d\lambda}$ is normalized downward flux for zero surface reflectance, equivalent to the total downward transmission, and T_λ is total upward transmission, s_λ is atmospheric backscattering ratio, and ρ_λ^s is surface reflectance. Note that for this equation, we assume that there is no ‘extra’ radiation arising from adjacent scenes (e.g., clouds) and that there is no absorption by trace gases. Also, note that this equation has been simplified for
325 readability, although all terms have angular dependence. Given a radiative transfer model (RTM), knowledge of the aerosol type and loading, one can calculate all properties of the atmospheric contribution (e.g., ρ_λ^a , $F_{d\lambda}$, T_λ , and s_λ).

By rephrasing Eq. (9), surface reflectance, ρ_λ^s , can be written as shown in Eq. (10). If the ρ_λ^* is the observation, and we somehow “know” the properties of the aerosol plus Rayleigh atmosphere (e.g., measured from AERONET), we can determine the ρ_λ^s . This process is known as AC, and the ρ_λ^s derived from Eq. (8) is referred to as AC-ref.

$$\rho_\lambda^s = (\rho_\lambda^* - \rho_\lambda^a) / (s_\lambda (\rho_\lambda^* - \rho_\lambda^a) + F_{d\lambda} T_\lambda) \quad (10)$$

The AC-ref is an estimate of that surface reflectance, obtained by using an RTM to ‘subtract’ the atmospheric contribution from observed TOA values. By calculating this surface reflectance in different wavelengths, we can determine the spectral relationships that we need for the DT aerosol retrieval algorithm.

Let us focus on performing AC for ABIE only and compare with corresponding AC using MODIS observations over the ABIE
335 domain. We assume that the TOA reflectance is the 10 km x 10 km Mean_Reflectance_Land parameter contained in the Level 2 aerosol product, which in turn corresponds to gas-absorption-corrected, cloud-masked and outlier-removed statistics of the original (Level 1B) spectral reflectance. The aerosol loading (e.g., spectral AOD) is observed by AERONET, and the RTM assumes the “Continental” (Remer et al., 2005) model to derive the spectral path reflectance and other atmospheric terms in Eq. (10). This process is summarized by the flowcharts in Fig. 4.

340 We need to atmospherically correct the blue, red and “2 μm ” (2.11 μm for MODIS or 2.25 μm for ABIE) band to obtain surface reflectance at those wavelengths. AERONET measures AOD at several wavelengths in the visible so we calculated the 2nd order polynomial fit of spectral AOD between visible and SWIR channels. Interpolating AOD to the specific blue and red bands for MODIS or ABIE introduces minimal error. However, since there are no AERONET AOD measurements near 2 μm , we must extrapolate. Among the 193 AERONET sites used for collocation, 169 of those sites have observations at 1.64
345 μm , so can we use a second order polynomial fit to estimate AOD at 2 μm with reasonable confidence. The second order fit



is also applied for 24 AERONET sites with the longest observation wavelength of 1.02 μm . In this case, the extrapolation may induce greater error in the AOD estimation. Meanwhile, we use the generic Continental (Remer et al., 2005) model that provides spectral scattering and absorption properties, including a one-to-one relationship between extinction at all wavelengths in question. Although there are still uncertainties, by restricting the AC to situations where AOD at 0.55 μm is
350 < 0.2 , assuming Continental model, and extrapolating AERONET AOD where possible, we reduce the uncertainty related to aerosol model assumption for deriving AC-ref.

Figure 5 shows scatter plots of AC-ref of different wavelengths obtained from the GSFC AERONET site from a year of ABIE observations. The AC-ref in the red wavelength (Fig. 5a) and blue wavelength (Fig. 5b) overall are strongly correlated with AC-ref in the SWIR and red, respectively, as currently assumed in the DT algorithm (Eq. 2). However, rather than being
355 constant, regressions for both wavelength pairs change with SZA and correlate poorly when SZA is very high ($> \sim 75^\circ$).

4.2 Testing the AC-ref to the DT algorithm

Here, we use the results in Fig 5, to test whether the SRPs help to improve the ABIE DT retrieval. Although the regression quality varies with SZA, to a first approximation we see that both red/SWIR, and blue/red vary nearly monotonically with SZA. We use this relationship to determine whether an SRP that includes SZA might improve the DT retrieval, at least at the
360 GSFC site. Figure 6 shows the results of this pilot study, using these new SRPs as compared with the AOD retrieved from the baseline SRPs at GSFC. Figure 6(a) shows correlations between the DT AODs and AERONET AODs, and Fig. 6(b) represents the biases in DT AODs for each hour. The baseline DT AOD correlates well with AERONET AOD with correlation coefficient of 0.91 but is positively biased with slope of 1.44 and y-intercept of 0.01. Diurnal bias variation reveals a peak near noon time, like the comparison shown in Fig. 3(a). This pilot study shows us that modification of SRPs varying with SZA mitigates the
365 bias peak at noon (Fig. 6b). The new AOD shows a significant improvement in that 92.62% of retrieval falls within expected error (%EE) range ($\pm 0.05 + 15\% \tau$) (Levy et al., 2013), compared to 50.82% of the baseline AOD falling within the %EE.

While there is circularity in this test, with validation being done with the formulation data set, there are many steps between formulation and validation and this test shows us (a) consistency through all those steps and (b) that changing the SRP assumption causes a response in the retrieval of the right order of magnitude to correct the bias.

370 5. Spectral Relation Parameterization

5.1 Comparison of SRP between MODIS and ABIE

To compare this study with the SRPs used now in the current MODIS algorithm and to derive new SRPs for ABIE we return to the large data base of AC-ref, where at each collocation spectral AC-ref is used to calculate parameters of the spectral AC-ref relationships.



375 On the basis of a physical connection between light absorption in visible wavelengths involved in photosynthesis and the
SWIR light absorbed by liquid water in vegetation, Kaufman et al. (1997a) observed correlation between visible (red, blue)
and SWIR surface reflectance as measured by low-flying aircraft and atmospherically corrected images from satellite and
high-flying sensors. These correlations were presented as simple ratios (blue and red reflectance is $\frac{1}{4}$ and $\frac{1}{2}$ of that in SWIR).
With AC of early MODIS data, Levy et al. (2007b) found that regressions indicated non-zero y-intercepts. Although it was
380 poorly understood why there should be non-zero intercepts, retaining the non-zero y-offsets for the SRP improved the aerosol
retrieval results. Figure 7(a) repeats the study of Levy et al. (2007b) with more recent data (2015-2019 and over the ABIE
region only), confirming the presence of non-zero offsets in the MODIS SRP. Even with a much-different sampling of
AERONET data in this (ABIE region only, different period) the overall red/SWIR and blue/red relationships are very similar
to the earlier regressions.

385 Figure 7(b) applies the same AC-ref technique but for the ABIE observations. While the slopes and y-offsets are overall
similar to those observed when regressing MODIS, there is increased scattering for both wavelength pairs, with significantly
reduced correlation in the blue/red relationship.

With MODIS, the variability in relationship between visible and SWIR AC-ref is controlled by parameterizing with
 $NDVI_{SWIR_LEO}$ and scattering angle as explained in Sect. 2.1. We repeat the entirety of the Levy et al. (2007b) study with the
390 newer MODIS data of the Western Hemisphere only, as well as with the ABIE data. The results are presented in Fig. 8 and
9, with panels (a) and (c) representing MODIS and panels (b) and (d) representing ABIE. The panels in Fig. 8 show changes
of overall ratios (forced through zero) when separated into three bins of $NDVI_{SWIR}$ ($NDVI_{LEO_SWIR}$ or $NDVI_{GEO_SWIR}$), whereas
the panels in Fig. 9 show the values of regression (slope and y-intercept) for each of 20 bins of scattering angle. AC-ref are
sorted according to scattering angle, binned into equal number bins and regression parameters are calculated for each bin. The
395 mean of each bin is plotted against a scattering angle.

For MODIS (e.g., Fig. 8(a), 8(c), 9(a) and 9(c)), the overall patterns remain similar to the equations shown in Sect. 2.1. In Fig.
8(a), the slope decreases from 0.60 to 0.52 with an increase of $NDVI_{SWIR}$ from 0.25 to 0.50 like Eq. (4). The blue-red slopes
are almost independent of $NDVI_{SWIR}$ (Fig. 8b), as in the current DT MODIS algorithm (Eq. 4). For scattering angle, the slope
and y-intercept change (Fig. 9a and 9c, red) with rate of decrease/increase not much different from those in Eq. (3). Note that
400 the SRPs described by Eq. (3) also include a term dependent on $NDVI_{SWIR}$ that is not explicitly accounted for in the Fig. 9
analysis, so exact dependencies on scattering angle are not expected to be identical. In Fig. 9(a), we see that indeed the
scattering angle dependence of parameters between blue and red is much weaker than their red-SWIR counterparts. In
conclusion, we find that the SRPs derived in this study from the MODIS AC-ref data base at AERONET stations in the western
hemisphere agrees within expectations with the dependence on scattering angle and $NDVI_{SWIR}$ being used in the current
405 MODIS DT algorithm that was derived years ago from a global database.



On the other hand, the spectral relationships of ABIE AC-ref are different from the MODIS ones. First, it is seen that the blue-
410 red relationship has a variability that cannot be expressed as a constant. In Fig. 8(d), slope between blue and red is significantly
higher when the $NDVI_{SWIR}$ is greater than 0.5. We also find clear scattering angle dependence in the slope and y-intercept for
the blue-red AC-ref relationship from Fig. 9(b and d, blue). It can be presumed that the blue-red correlations show greater
scatter in Fig. 7(b) and Fig. 8(b) due to the changes of spectral relationship with viewing geometry.

While the change in slope between the red and SWIR AC-ref by $NDVI_{SWIR}$ (Fig. 8b) shows the similarity with the MODIS
415 relationship, in Fig. 9(b), its dependency on scattering angle presents differently. Unlike the MODIS slope that increases
linearly with the increase of the scattering angle, the ABIE slope shows a weak scattering angle dependence. In particular,
when the scattering angle is higher than $\sim 150^\circ$, the slope is significantly lower than that of MODIS. Since the angle dependence
shown in Fig. 9(a) is sufficiently similar to the current DT assumption, comparing Fig. 9(a) and Fig. 9(b) shows that the current
SRP overestimates red slope and underestimates the blue slope when the scattering angle is high. This in turn leads to high
420 bias in backscattered conditions near noon as shown in Fig. 3.

There are multiple possibilities for the large differences between ABIE and MODIS SRP parameters. One is that the
wavelengths are different. MODIS blue, red, and SWIR channels are centered near $0.466 \mu\text{m}$, $0.654 \mu\text{m}$ $2.113 \mu\text{m}$, while
corresponding ABIE channels are centered near 0.470 , 0.639 and $2.256 \mu\text{m}$, respectively. To test the impact of the wavelength
shift, we used surface reflectance obtained from ASTER spectral library (Baldrige et al., 2009) that includes 2300 spectra of
425 a wide variety of materials covering $0.35\text{--}2.5 \mu\text{m}$ with 0.001 nm resolution. We integrated bidirectional reflectance from 340
vegetation tree and 174 vegetation shrub cases for the specific wavelength pairs of each MODIS and ABI. The conclusion was
that the wavelength shifts from MODIS to ABI results in negligible differences in red-SWIR relationship, while the blue-red
slope decreases by 10% from 0.86 to 0.77 and the y-intercept increases from 0.001 to 0.003. These differences are not large
enough to explain the differences between ABIE and MODIS SRP, as seen in Fig. 9.

430 The second and more likely reason for the differences is that ABIE and MODIS have very different viewing geometries, as
discussed in Sect. 3.1. While the scattering angle parameterization in the MODIS and baseline ABIE algorithm is meant to
adjust the SRP parameters to account for anisotropic reflectance effects, spectral anisotropy is obviously more complex than
can be modeled by a single parameter (e.g., Gatebe and King, 2016). ABIE's coupling of view angle with location has
apparently accentuated the biases remaining from the one parameter formulation, while MODIS' mixing of view angles over
435 each location has mitigated these biases. Note that Remer et al. (2001) find strong view angle dependence in observed ratios
of visible to SWIR, but that averaging over the range of view angles would bring observed ratios closer to the $\frac{1}{4}$ and $\frac{1}{2}$ values
expected at the time of their study. The Remer et al. (2001) study also found dependencies on land surface type and season.

5.2. Surface Reflectance Parameterizations for ABI-East.

5.2.1 Land Type

440 In Sect. 5, we discussed that, for ABIE observations, variability between visible and SWIR AC-ref (Fig. 7b) does not clearly
depend on scattering angle. Spectral AC-ref relationships change with solar angles at a given location (e.g., Fig. 5) but appear



different at different sites. Therefore, we explore whether there may be other parameters to explain surface reflectance relationships. One possibility is to use a more explicit parameterization based on surface type.

445 The DT SRP attempts to account for land cover type (and seasonal changes) using the $NDVI_{SWIR}$ (Eq. 4) and scattering angle (Eq. 3) as a proxy for bidirectional reflectance. This appears to be sufficient for MODIS, where SZAs and vegetation conditions both co-vary on seasonal scales. Differences in day-to-day viewing geometry help to remove overall biases caused by the SRP. Nonetheless, there was enough remaining bias over non-uniform and isolated urban surfaces that the MODIS-DT retrieval added a correction based on urban percentage (Gupta et al., 2016).

450 The ABIE geometry presents a very different problem in that every ground location is isolated – there is no ‘averaging’ of viewing angle. In fact, the definition of BRDF requires a fixed SZA, and that SZA varies throughout every day. Thus, unlike MODIS (or another LEO sensor), one may not be able to assume a generalized dependence on the scattering angle for all ground target locations. Of course, the pathological limit is that there is a unique BRDF and functional dependence of solar angle at every location viewed by ABIE. Developing this “map”, however, would be extremely expensive (time and computationally), and would require similar efforts to develop these descriptions for ABIW, AHI and any future regionally
455 observing geostationary imagers. Therefore, we attempt to simplify this problem by separating the globe into three canopy types (two vegetation types plus urban) that represent the darker surfaces used for DT retrieval. From there, we develop a three-tiered SRP and test whether that can be used for ABIE and other GEO sensors.

According to the IGBP index, we classify surfaces dominated by deciduous or evergreen Forest (IGBP index 1 ~ 4) as Closed Vegetation (CV) and other vegetation (IGBP index 5~10, 12, 14) as Open Vegetation (OV). Figure 10 shows the global map
460 of IGBP index and percentage of each land cover type (%land type) at $0.1 \times 0.1^\circ$ resolution, which are obtained from the MCD12Q1 products at 500 m resolution. By counting individual IGBP indices from all sub grid pixels, we obtain the most frequent IGBP index (Fig. 10a) and percentage of CV (Fig. 10b), OV (Fig. 10c) and urban (Fig. 10d) in a grid box. Using 20% to be the threshold that determines dominant type in the grid box, OV dominates over most of the global land mass. CV is dominant in 17.6% of non-water, ice-free, and non-barren pixels, and is generally concentrated near the equator. Meanwhile,
465 the urban is dominant in 0.7% of the situations and is sporadically distributed. While determining the dominant type in each grid box allows us to create the global maps of Fig. 10, it is the percentage of each type in the grid box that will be used to weight each of the three surface reflectances corresponding to the results of the three SRP applied to each grid box with multiple surface types within.

Figure 10 shows that multiple land types can exist simultaneously in a grid box in most cases where the surface properties are
470 not uniform over a wide range. Since AC-ref is based on the contribution from each type, it can be assumed that the spectral AC-ref relationship is dependent on the %land type of the area for which the AC-ref is calculated, just as the urban percentage changes the SRP in the current algorithm. We intend to create an SRP for each land type, Open and Closed Vegetation, in the same manner that urban percentage is used in the current DT algorithm. We will do this in two steps. First, we develop the land type’s SRP. Second, we apply the new SRP to the retrieval.



475 To derive the slope and y-intercept change by % land type, the SRP analysis allows multiple land types for a single collocation
and does not throw out heterogeneous conditions. Thus, an AERONET site can be assigned to different land types
simultaneously for the derivation. For example, if we assume for the derivation that an AERONET site is covered by 20%
urban, 50% CV and 30% OV. The Red/SWIR relationships obtained from the site then will show up in Fig. 12 b, d, and f, and
will correspond to different x-location of 20%UP, 50%CV, and 30%OV. When the AERONET site is covered by 100% CV,
480 then it will be only in Fig. 12b. In this manner, we derived dependency of spectral relationships on %land type from Fig. 12.
In the retrieval process, the algorithm now assumes a homogenous surface, even when the surface is heterogeneous. The
algorithm reads the %land type maps (Fig. 10) and identifies the highest percentage land type in each pixel. The algorithm
uses open vegetation by default and adjusts the SRP where the %CV or %UP is higher than the %OV. For the case of 20%UP,
50%CV, and 30%OV case, the algorithm chooses CV and calculates the SRP for 50% CV by using the multiple linear
485 regression described in Sect. 5.2.2. The contribution of the other 50% of the pixel is not considered here. Accordingly, the
following unfortunate case will be possible. If the pixel is filled with 40%CV, 30%OV, and 30%urban, the pixel is identified
as CV even though 60% of pixel is covered by other types. Ideally, a weighting function that takes into account significant
percentages of all surface categories would be preferable and such a weighting function will be investigated in a subsequent
study. This section describes the process of creating the SRP's specific to each land type, leaving further description of the
490 application of SRP to Section 6.1.

In Fig. 11, we plot the Red and SWIR AC-ref relationship by land type. A population of AC-ref shown by gray dots were
categorized into three group as described before, and a linear regression was fitted for each AC-refs group. AC-ref in each
group were binned into 10 equal bins, and the mean and standard deviation of each bin was calculated and shown by colored
circles and vertical bars. The CV is dark at both SWIR and red wavelengths and has a lower slope compared to the OV and
495 urban. Meanwhile, for urban, red AC-ref to SWIR AC-ref ratio across the entire dynamic range of reflectance is higher than
the other land surface types, causing a higher y-intercept than the other two groups. Since OV encompasses all the various
land cover types that are not classified as CV or Urban and dominates the statistics, the regression of this type is similar to the
overall correlation where no surface type is specified, as shown in Fig. 7 (b, red). In Fig. 12 we look for dependencies of the
regression slope by plotting the slope against $NDVI_{SWIR}$ and the different land cover type percentages. In this figure, we see
500 that the slope of the CV group depends on %CV (Fig. 12b) rather than $NDVI_{SWIR}$ (Fig. 12a), while the opposite is true for the
OV group. Again, we note that the OV group dominates the overall statistics so that we expect the parameters of the OV
group to behave much more like the current assumptions in the algorithm than the other two groups. The urban slope decreases
as $NDVI_{SWIR}$ increases but increases as %urban increases. In short, in typical vegetation, slopes from the red-SWIR regression
range between 0.4 to 0.7, and slope variability is well captured by parameterization using $NDVI_{SWIR}$. When the surface
505 becomes even darker, as in CV, the regression loses its sensitivity to the $NDVI_{SWIR}$ and becomes dependent on forest coverage.



5.2.2 Multiple Linear Regression for Red and SWIR relationship

510 Previously, we discussed the inability to parameterize the angular dependence of the SRP with only scattering angle in the same way as is done with the current MODIS DT algorithm (Fig. 9). We also discussed that the correlation between visible and SWIR AC-ref obtained from ABIE varies with land cover type (Fig. 11) and investigated a dependency on NDVI_{SWIR} and %land type (Fig. 12). Based on the above analysis, for the red and SWIR relationship, we introduce a new SRP that takes into account SZA, NDVI_{SWIR} and %land types through multiple linear regression. In this way, anisotropic reflectance is
515 parameterized as a function of SZA as before, but that relationship is modified simultaneously by NDVI_{SWIR} and %land. Also, the urban correction is no longer being performed as an add-on process as it is in the current MODIS DT algorithm.

Like the current MODIS DT algorithm, this study aims to parameterize the regression coefficients of spectral relationships of surface reflectance. We predict the slope and y-intercept as a function of input parameters and then derive the red surface reflectance from the SWIR surface reflectance based on those coefficients. Table 1 summarizes the multiple linear regression
520 (MLR) between input parameters and the coefficients for each land type. Each MRL coefficient listed in the table represents the change in predicted value per unit change in the predictor, holding all other input variables constant. The constant is equal to the predicted value when all the input parameters are zero. That is, according to the MLR coefficient, the key factor to change the spectral relationship is NDVI_{SWIR} for OV and urban, but it can be seen that %land type plays an important role in CV and urban conditions as illustrated in Fig. 12. Note that while the MLR coefficients for SZA seem small, the value of SZA
525 ranges from 0 to 70, whereas the value of NDVI_{SWIR} and %land ranges from 0 to 1. Multiplying MLR coefficients by typical values can place the influence of SZA on the same scale as the land parameters.

5.2.3 New SRP for Blue and Red relationship

The Blue and Red relationship does not change significantly with land type. We account only for the NDVI_{SWIR} dependence and angular change which are shown in Fig. 8 and Fig. 9. The blue and red relationship is parameterized as a linear function
530 of scattering angle for three NDVI_{SWIR} groups as shown in Fig. 13.

In Fig. 13, the ratio of blue to red is close to 0.6 under backscattering conditions and is not significantly distinguished according to NDVI_{SWIR}. The blue-red relationship of the three NDVI_{SWIR} groups is differentiated in terms of dependence on the scattering angle. The slope decreases slightly as the scattering angle decreases when NDVI_{SWIR} is lower than 0.5, whereas when NDVI_{SWIR} is high, the transition from backward to forward scatter increases the slope. It is seen that the ratio is as high as 1
535 under forward scattering condition. The high NDVI_{SWIR} mostly corresponds to the dense vegetation such as tropical forests and crops at their peak growth status. The forest canopy induces shadow-driven reflectance in forward scattering, which darkens blue and red reflectance and consequently a 1 to 1 regression between them.



6. Result

6.1. Applying the new SRP in the DT algorithm

540 The newly developed SRPs are applied to the DT algorithm for ABIE, and performance is tested in terms of predicted surface reflectance and retrieved AOD. The visible surface reflectances predicted from the AC-ref at the SWIR wavelength obtained from ABIE observation are compared to the visible AC-ref in Sect. 6.2, and the AODs retrieved from the modified DT algorithm for ABIE by adopting the new SRPs are validated with AERONET AOD in Sect. 6.3.

The ABIE-DT algorithm follows the same flow as described in Sect. 2.1 but assumes the new SRP for both red and blue
545 surface reflectance estimation. As different SRP assumptions are made depending on the land cover type, a classification of land type is performed based on an ancillary map of %CV, %OV and %urban before estimating the surface reflectance. Considering the 10 km resolution of DT retrieval, we applied the map of %land type derived from a 0.1 x 0.1° grid box in the same manner as we used to produce the maps in Fig. 10. The classification process finds the %CV, %OV and %urban from the nearest grid box for each location, then assigns the pixel to be CV or urban if the %CV or %urban is higher than others. In
550 case of equal percentage of two different type in a grid, we put priority in order of urban, CV, and OV. For example, if both %CV and %urban occupies 40% of the area respectively, the pixel is assigned as urban. If none of conditions are met, the DT retrieval assumes OV as the default.

6.2. Comparison of predicted surface reflectance

Figure 14 shows the comparison between the predicted surface reflectance and AC-ref in blue and red, respectively. It also
555 compares the performance of the new SRP to that of the baseline SRP applied to the MODIS DT algorithm. In Fig. 14(a), it is seen that the baseline SRP overestimates the red surface reflectance in CV but underestimates it in OV. In urban, the predicted surface reflectance correlates closely with AC-ref, but with a higher root-mean-square error (RMSE) than other land types. The surface reflectance predicted by the new SRP (Fig. 14b) represents a smaller RMSE in CV and urban compared to the baseline product. It is also bringing the predicted surface reflectances closer to the atmospherically corrected values. When it
560 comes to prediction of blue surface reflectance, both the baseline and new SRP produce estimated surface reflectances that underestimate AC-ref, but the new SRP lowers the RMSE relative to the original values for all land surface types.

There is a degree of circularity in comparing the resulting estimated surface reflectances to the same data from which they were derived. However, many factors come into play during the derivation and there is no guarantee that estimated reflectances will match the AC-ref any better than those derived from the baseline SRP. However, the first basic step is to prove that the
565 estimated reflectances do indeed match the statistics of their formulation data set. As such the results presented in this section are a necessary but not comprehensive proof of the new parameterization.



6.3. Comparison of DT-GEO AOD and AERONET AOD

The goal of the new SRP is not to derive surface reflectance, but to improve the AOD retrieval from GEO observations. Therefore, we use the new SRP in the DT algorithm applied to ABIE, which provided the formulation data set, but also its
570 sister sensor ABIW, which remained independent of the derivation.

Figure 15 shows the new GEO DT AOD retrieval from ABIE on September 6th, 2019, with 3-hour interval between 13 and 22 UTC. An aerosol plume crossing from north to south over Missouri is captured from the retrieval (Fig. 15. a-d), and other small plumes are detected around Houston and Louisiana as well. We select two AERONET sites adjacent to the aerosol path and compare the new AOD with the baseline AOD and AERONET AOD (Fig. 15e and f). At NEON_KONZ [39.10°N, -
575 96.56°E], both the baseline and the new AOD follows the decreasing AERONET AOD between 14 and 23 UTC, albeit with a positive bias. The AOD at IMPROVE_MammothCave [37.13°N, -86.15°E] is as low as 0.1 at 13 UTC, but consistently increases as the aerosol plume approaches and peak at 23 UTC. Comparing the DT AODs, the new AODs are mostly lower than the baseline AODs, especially during local noon hours (17~19 UTC).

The initial issue with the DT algorithm applied to ABI sensors data was shown in Fig. 3 where we noticed an overall high bias that became maximum at around noon. Figure 16 illustrates the mitigation of the diurnal signature of the high AOD bias when
580 applying the new SRP. The red dots recreate the original diurnal pattern from Fig. 3, and the black dots are the result of the new SRPs. The bias from AERONET of the new retrieved AOD is lower and less time dependent than the original. Although the new SRP was developed using AC-refs obtained from ABIE, applying the new SPR to the ABIW DT retrieval also mitigates the high AOD bias around noon as shown in Fig. 16(b). Thus, the ABIW results provide independent validation of
585 the success of the new SRPs.

Figure 17 displays the average bias of the retrieved AOD against AERONET at each AERONET site. Figure 17(a and b) are side by side comparisons of the results of the old and new SRPs, respectively for ABIE. The products of ABIW are compared in Fig. 17(c and d). The ABIE AOD retrieved from the MODIS DT algorithm (Fig. 17a) agree with AERONET AOD with differences ranging between 0.0~0.2 at most stations. The positive bias is also prominent in ABIW AOD across western North
590 America. Figure 17(b and c) show that the retrievals using the new SRP decrease the bias in both ABIE and ABIW AOD. However, the GEO-DT algorithm still overestimates AOD across most of western North America and some random locations. At some locations across the region, a positive bias turns into a negative one, but not below -0.05. The overall picture is one of improvement with stations closest to the subsatellite point with the smallest SZA at noon seeing the largest success.

7. Discussion

595 The DT algorithm does not require building a database of surface reflectance using several years of satellite observations and thus is quickly adaptable to new sensors. This is because it constrains surface reflectance dynamically in real-time. The constraint is based on a physical connection between light absorption in the visible and SWIR in plant leaves and bare soil.



The physical connection leads to empirically derived spectral relationships between surface reflectance in different bands. The surface reflectance parameterization (SRP) approach can be valid for any sensor. However, differences in viewing geometries
600 between LEO and GEO sensors introduced an issue in the SRP parameterization. We explore this issue by calculating surface reflectance from top-of-atmosphere reflectance measured by a LEO sensor (MODIS) and a GEO sensor (ABIE) using atmospheric correction at AERONET sites.

In the MODIS case, using the most recent 5 years of observations confirmed the same SRPs and the same dependency on scattering angle established 20 years ago. However, an assessment of ABIE AC-ref determined that the GEO SRPs were
605 inconsistent with the MODIS-based SRPs. At the outset these differences could be attributed to either spectral differences in the wavelength bands of each instrument or to the viewing geometry differences between a LEO and GEO. A sensitivity study proved that spectral differences cannot explain the magnitude of the differences that we are seeing. However, a remarkable difference between the SRPs of MODIS and ABIE was seen in the dependence on the scattering angle, which suggests geometrical differences play a significant role. The inconsistency increases bias in visible surface reflectance when the
610 scattering angle is higher than 150° . We note that for ABIE, the relative azimuth angle (RAA) range at each site spans 40° to 180° . Meanwhile, the MODIS RAAs are limited to two sectors: 40° to 70° and 120° to 150° . For MODIS, within each sector the variety of VZA encountered dilutes geometrical differences for average values. Most importantly MODIS never measures $RAA > 150^\circ$, near the vegetative hotspot.

The key to the differences between MODIS and ABIE is based on the fact that GEO and LEO measurements have different
615 viewing geometries, and changes in scattering angles are driven by different factors in each sensor. In ABIE, solar angle varies, but VZA stays constant at each location, while MODIS measures a narrow range for solar angle while observing a wide range of VZA. This has two implications. First, for ABIE, because VZA is constant at each site, geometry is convolved with surface characteristics such as land cover. Thus, a dependence of SRP on the scattering angle in the ABIE analysis may be a proxy for land cover type. Second, ABIE encounters different combinations of VZA, SZA, and RAA that MODIS never does. The
620 baseline parameterization appears to continue to serve DT MODIS well, suggesting that the decreased ability of the baseline parameterization to serve ABIE may lie in the new geometrical combinations that are now appearing in ABIE.

The connection to the vegetative hot spot as the source of the differences in the spectral relationships of MODIS and ABIE suggests that ignoring surface cover characteristics could be the root cause of lingering uncertainties in the MODIS DT SRP and the reason for ABIE's poor performance. One way to illustrate the convolution between geometry and surface properties
625 in the ABIE data is to examine in detail the situation in differing land covers. Figs 11 and 12 demonstrate that AC-refs classified into Open Vegetation (OV), Closed Vegetation (CV), and Urban have different spectral relationships. The regression coefficients between red and SWIR AC-ref vary with land cover type and show dependence according to the homogeneity of land cover and $NDVI_{SWIR}$. The blue and red spectral relationship does not differ significantly depending on the land cover, but unlike the DT MODIS relationship, the variability according to the $NDVI_{SWIR}$ is evident.

630 We note that even the LEO DT algorithm began to explicitly address land cover type in its SRP when that land cover was Urban beginning with Collection 6.1 but continued to group all vegetation types together. However, with GEO, the novel



geometry that includes the vegetation hotspot and convolves VZA with a specific location requires separate SRP for at least two vegetation categories.

8. Conclusion

635 The new GEO sensors: Advanced Himawari Imager (AHI) on the Himawari satellite, the Advanced Baseline Imagers (ABIs) on the GOES- East and GOES-West sensors, the Advanced Meteorological Imager (AMI) on the Geostationary Korea Multi-Purpose Satellite - 2A offer the aerosol community unprecedented opportunity to explore the temporal characteristics of aerosol with applications for air quality monitoring, resolving a developing smoke plume near its fire source, the co-evolution of aerosols and convective clouds on time scales of the convection and other possibilities. However, the same robust aerosol product that the community has come to expect from MODIS and VIIRS must be produced from the GEO sensors. Most importantly, any biases found in the retrieved AOD must be diurnally constant otherwise the very phenomena of interest to the community can be aliased by the diurnal signature in the error of the product.

We began this study with a baseline version of the DT-algorithm for GEO sensors including ABI. This includes lookup tables that account for shifted wavelengths, and modifications to cloud masking due to different resolutions and missing wavelengths.

645 Based on our experience with porting to VIIRS, we assumed that the SRPs used for MODIS would be appropriate for the GEO sensors. Previous to this study, initial evaluation of the baseline GEO algorithm applied to AHI showed a correlation with collocated AERONET AOD and mean bias and RMSE only a little less accurate than MODIS AOD at the same stations and time period (Gupta et al., 2019). These were encouraging results that propelled the baseline GEO algorithm to be applied to ABIE and ABIW with the same SRPs and for the resulting ABI AOD to be included in a global product consisting of AOD derived from three GEO sensors and three LEO sensors (Gupta et al., personal communication). Initial validation of ABIE and ABIW, as part of this merged product, show overall validation statistics comparable to MODIS, especially in terms of the percentage within expected error (%EE), but with a higher bias (Gupta et al., personal communication).

In this study we specifically examined the diurnal signature of differences with collocated AERONET AOD and found a distinctive diurnal signature of the bias with an amplitude of 0.10. The work done in the present study has focused on reducing the diurnal signature of the AOD bias against AERONET, which will strengthen the applicability of the DT ABI products for characterization of aerosol diurnal properties. While the baseline algorithm produces a robust and reasonable global product, by developing a new SRP from ABIE atmospherically corrected reflectances we may be able to cut the overall positive biases in half to 0.01 to 0.08 and more importantly flatten the amplitude of the diurnal signature to less than 0.05. The new SRP parameterization was applied to ABIE measurements, the same data set that was used for its formulation, but it was also tested with ABIW measurements that provide an independent verification. The ABIE results are slightly better than ABIW results, as expected, but the independent ABIW results conform to the same error bars described above: a positive bias of less than 0.08 and a flattened diurnal signature with amplitude less than 0.05. We have not applied this new SRP to AHI or other GEO satellite sensors. Because AHI views a different part of the globe with different vegetation, topography and soil types than do



the ABI sensors, this specific parameterization fine-tuned for the Americas may not work as well for AHI's view of Asia and
665 Oceania. With all their temporal promise, GEO sensors are essentially regional instruments by definition. It is possible that
to maximize capability of each GEO sensor individual parameterizations may be necessary and regional versions of the DT
algorithm more appropriate. A balance must be found between regional tuning and the goal of maintaining global consistency
so as not to lose the ability to characterize the global aerosol system as a whole.

The investigation of the validity of applying the SRPs developed here for AHI and the question of balancing regional tuning
670 with a global perspective are beyond the scope of this study. For now, we have a robust algorithm for the over land retrieval
of aerosol that can be applied to the ABI instruments. The algorithm's parameterizations are based on understood physics of
spectral light absorption and scattering by vegetative canopies. The parameterization described here will be implemented into
the DT package, available ABI observations will be processed, and the product made publicly available.

Data availability

675 The Dark Target (DT) algorithm has been ported to ABIs and produces aerosol data as part of the NASA MEaSUREs project
(ROSES-2017; <https://www.earthdata.nasa.gov/esds/competitive-programs/measures/leo-geo-synergy>), and the products will
be publicly available soon. The NOAA GOES-R Series Advanced Baseline Imager (ABI) Level 1b Radiances can be accessed
via doi:10.7289/V5BV7DSR (NOAA NCEI; GOES-R Calibration Working Group and GOES-R Series Program, 2017). The
AERONET direct sun measurement data used in this study are available via the AERONET website
680 (https://aeronet.gsfc.nasa.gov/new_web/download_all_v3_aod.html, AERONET team, 2023; Giles et al., 2019). MODIS Land
Cover Type (MCD12Q1) version 6 products (DOI: 10.5067/MODIS/MCD12Q1.061) can be accessed via LAADS DAAC
(<https://ladsweb.modaps.eosdis.nasa.gov/>, last access: June 2023).

Author contributions

MK, RL, and LR designed this study. MK and SM developed retrieval codes and carried the experiments; MK, RL, and LR
685 analyzed the data and result. PG guided land type percentage calculation. MK prepared the manuscript draft, and it was
reviewed by all authors.

Competing interests

The contact author has declared that none of the authors has any competing interests.

References

690



- Al-Saadi, J., Szykman, J., Pierce, R. B., Kittaka, C., Neil, D., Chu, D. A., Remer, L., Gumley, L., Prins, E., Weinstock, L., MacDonald, C., Wayland, R., Dimmick, F., and Fishman, J.: Improving National Air Quality Forecasts with Satellite Aerosol Observations, *Bull. Am. Meteorol. Soc.*, 86, <https://doi.org/10.1175/BAMS-86-9-1249>, 2005.
- Baldridge, A. M., Hook, S. J., Grove, C. I., and Rivera, G.: The ASTER spectral library version 2.0, *Remote Sens. Environ.*, 695 113, <https://doi.org/10.1016/j.rse.2008.11.007>, 2009.
- Belward, A. S., Estes, J. E., and Kline, K. D.: The IGBP-DIS global 1-km land-cover data set DISCover: A project overview, *Photogramm. Eng. Remote Sensing*, 65, 1013–1020, 1999.
- Boucher, O., Randall, D., Artaxo, P., Bretherton, C., Feingold, G., Forster, P., Kerminen, V.-M., Kondo, Y., Liao, H., Lohmann, U., Rasch, P., Satheesh, S. K., Sherwood, S., Stevens, B., and Zhang, X. Y.: Clouds and Aerosols, in: *Climate Change 2013 – The Physical Science Basis*, Cambridge University Press, <https://doi.org/10.1017/CBO9781107415324.016>, 700 2014.
- Chu, D. A., Kaufman, Y. J., Ichoku, C., Remer, L. A., Tanré, D., and Holben, B. N.: Validation of MODIS aerosol optical depth retrieval over land, *Geophys. Res. Lett.*, 29, <https://doi.org/10.1029/2001GL013205>, 2002.
- Chu, D. A., Kaufman, Y. J., Zibordi, G., Chern, J. D., Mao, J., Li, C., and Holben, B. N.: Global monitoring of air pollution 705 over land from the Earth Observing System-Terra Moderate Resolution Imaging Spectroradiometer (MODIS), *J. Geophys. Res. Atmos.*, 108, <https://doi.org/10.1029/2002JD003179>, 2003.
- Eck, T. F., Holben, B. N., Reid, J. S., Dubovik, O., Smirnov, A., O'Neill, N. T., Slutsker, I., and Kinne, S.: Wavelength dependence of the optical depth of biomass burning, urban, and desert dust aerosols, *J. Geophys. Res. Atmos.*, 104, <https://doi.org/10.1029/1999JD900923>, 1999.
- 710 Gatebe, C. K. and King, M. D.: Airborne spectral BRDF of various surface types (ocean, vegetation, snow, desert, wetlands, cloud decks, smoke layers) for remote sensing applications, *Remote Sens. Environ.*, 179, <https://doi.org/10.1016/j.rse.2016.03.029>, 2016.
- Giles, D. M., Sinyuk, A., Sorokin, M. G., Schafer, J. S., Smirnov, A., Slutsker, I., Eck, T. F., Holben, B. N., Lewis, J. R., Campbell, J. R., Welton, E. J., Korkin, S. V., and Lyapustin, A. I.: Advancements in the Aerosol Robotic 715 Network (AERONET) Version 3 database – automated near-real-time quality control algorithm with improved cloud screening for Sun photometer aerosol optical depth (AOD) measurements, *Atmos. Meas. Tech.*, 12, <https://doi.org/10.5194/amt-12-169-2019>, 2019.
- Gupta, P., Levy, R. C., Mattoo, S., Remer, L. A., and Munchak, L. A.: A surface reflectance scheme for retrieving aerosol optical depth over urban surfaces in MODIS Dark Target retrieval algorithm, *Atmos. Meas. Tech.*, 9, 3293–3308, 720 <https://doi.org/10.5194/amt-9-3293-2016>, 2016.
- Gupta, P., Levy, R. C., Mattoo, S., Remer, L. A., Holz, R. E., and Heidinger, A. K.: Applying the Dark Target aerosol algorithm with Advanced Himawari Imager observations during the KORUS-AQ field campaign, *Atmos. Meas. Tech.*, 12, <https://doi.org/10.5194/amt-12-6557-2019>, 2019.



- Kanakidou, M., Myriokefalitakis, S., and Tsigaridis, K.: Aerosols in atmospheric chemistry and biogeochemical cycles of
725 nutrients, *Environ. Res. Lett.*, 13, <https://doi.org/10.1088/1748-9326/aabccb>, 2018.
- Kaufman, Y. J. and Remer, L. A.: Detection of forests using mid-IR reflectance: an application for aerosol studies, *IEEE Trans. Geosci. Remote Sens.*, 32, <https://doi.org/10.1109/36.297984>, 1994.
- Kaufman, Y. J., Tanré, D., Remer, L. A., Vermote, E. F., Chu, A., and Holben, B. N.: Operational remote sensing of
730 tropospheric aerosol over land from EOS moderate resolution imaging spectroradiometer, *J. Geophys. Res. Atmos.*, 102, <https://doi.org/10.1029/96JD03988>, 1997a.
- Kaufman, Y. J., Wald, A. E., Remer, L. A., Bo-Cai Gao, Rong-Rong Li, and Flynn, L.: The MODIS 2.1- μm channel-
correlation with visible reflectance for use in remote sensing of aerosol, *IEEE Trans. Geosci. Remote Sens.*, 35, <https://doi.org/10.1109/36.628795>, 1997b.
- Kim, J., Jeong, U., Ahn, M.-H., Kim, J. H., Park, R. J., Lee, H., Song, C. H., Choi, Y.-S., Lee, K.-H., Yoo, J.-M., Jeong, M.-
735 J., Park, S. K., Lee, K.-M., Song, C.-K., Kim, S.-W., Kim, Y. J., Kim, S.-W., Kim, M., Go, S., Liu, X., Chance, K., Chan
Miller, C., Al-Saadi, J., Veihelmann, B., Bhartia, P. K., Torres, O., Abad, G. G., Haffner, D. P., Ko, D. H., Lee, S. H., Woo,
J.-H., Chong, H., Park, S. S., Nicks, D., Choi, W. J., Moon, K.-J., Cho, A., Yoon, J., Kim, S., Hong, H., Lee, K., Lee, H., Lee,
S., Choi, M., Veeckind, P., Levelt, P. F., Edwards, D. P., Kang, M., Eo, M., Bak, J., Baek, K., Kwon, H.-A., Yang, J., Park, J.,
Han, K. M., Kim, B.-R., Shin, H.-W., Choi, H., Lee, E., Chong, J., Cha, Y., Koo, J.-H., Irie, H., Hayashida, S., Kasai, Y.,
740 Kanaya, Y., Liu, C., Lin, J., Crawford, J. H., Carmichael, G. R., Newchurch, M. J., Lefter, B. L., Herman, J. R., Swap, R. J.,
Lau, A. K. H., Kurosu, T. P., Jaross, G., Ahlers, B., Dobber, M., McElroy, C. T., and Choi, Y.: New Era of Air Quality
Monitoring from Space: Geostationary Environment Monitoring Spectrometer (GEMS), *Bull. Am. Meteorol. Soc.*, 101,
<https://doi.org/10.1175/BAMS-D-18-0013.1>, 2020.
- Levy, R. C., Remer, L. A., Martins, J. V., Kaufman, Y. J., Plana-Fattori, A., Redemann, J., and Wenny, B.: Evaluation of the
745 MODIS Aerosol Retrievals over Ocean and Land during CLAMS, *J. Atmos. Sci.*, 62, <https://doi.org/10.1175/JAS3391.1>,
2005.
- Levy, R. C., Remer, L. A., and Dubovik, O.: Global aerosol optical properties and application to Moderate Resolution Imaging
Spectroradiometer aerosol retrieval over land, *J. Geophys. Res. Atmos.*, 112, <https://doi.org/10.1029/2006JD007815>, 2007a.
- Levy, R. C., Remer, L. A., Mattoo, S., Vermote, E. F., and Kaufman, Y. J.: Second-generation operational algorithm: Retrieval
750 of aerosol properties over land from inversion of Moderate Resolution Imaging Spectroradiometer spectral reflectance, *J. Geophys. Res. Atmos.*, 112, <https://doi.org/10.1029/2006JD007811>, 2007b.
- Levy, R. C., Remer, L. A., Kleidman, R. G., Mattoo, S., Ichoku, C., Kahn, R., and Eck, T. F.: Global evaluation of the
Collection 5 MODIS dark-target aerosol products over land, *Atmos. Chem. Phys.*, 10, <https://doi.org/10.5194/acp-10-10399-2010>, 2010.
- 755 Levy, R. C., Mattoo, S., Munchak, L. A., Remer, L. A., Sayer, A. M., Patadia, F., and Hsu, N. C.: The Collection 6 MODIS
aerosol products over land and ocean, *Atmos. Meas. Tech.*, 6, <https://doi.org/10.5194/amt-6-2989-2013>, 2013.



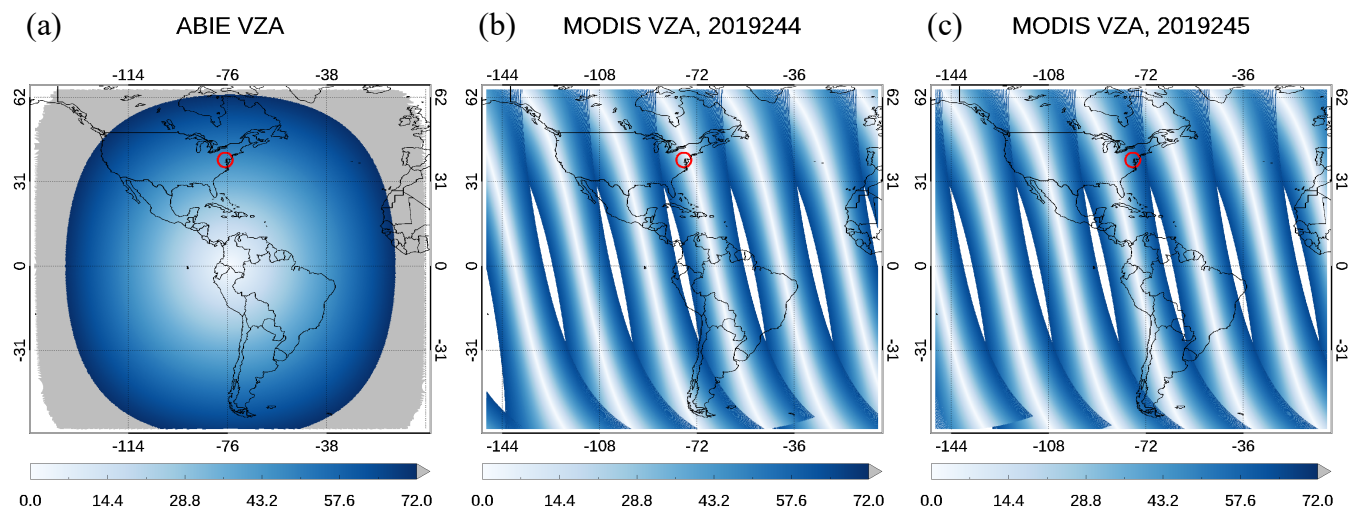
- Levy, R. C., Munchak, L. A., Mattoo, S., Patadia, F., Remer, L. A., and Holz, R. E.: Towards a long-term global aerosol optical depth record: applying a consistent aerosol retrieval algorithm to MODIS and VIIRS-observed reflectance, *Atmos. Meas. Tech.*, 8, <https://doi.org/10.5194/amt-8-4083-2015>, 2015.
- 760 Miura, T., Huete, A. R., van Leeuwen, W. J. D., and Didan, K.: Vegetation detection through smoke-filled AVIRIS images: An assessment using MODIS band passes, *J. Geophys. Res. Atmos.*, 103, <https://doi.org/10.1029/98JD00051>, 1998.
- Patadia, F., Levy, R. C., and Mattoo, S.: Correcting for trace gas absorption when retrieving aerosol optical depth from satellite observations of reflected shortwave radiation, *Atmos. Meas. Tech.*, 11, <https://doi.org/10.5194/amt-11-3205-2018>, 2018.
- Remer, L. A., Wald, A. E., and Kaufman, Y. J.: Angular and seasonal variation of spectral surface reflectance ratios: 765 implications for the remote sensing of aerosol over land, *IEEE Trans. Geosci. Remote Sens.*, 39, <https://doi.org/10.1109/36.905235>, 2001.
- Remer, L. A., Kaufman, Y. J., Tanré, D., Mattoo, S., Chu, D. A., Martins, J. V., Li, R.-R., Ichoku, C., Levy, R. C., Kleidman, R. G., Eck, T. F., Vermote, E., and Holben, B. N.: The MODIS Aerosol Algorithm, Products, and Validation, *J. Atmos. Sci.*, 62, <https://doi.org/10.1175/JAS3385.1>, 2005.
- 770 Remer, L. A., Kleidman, R. G., Levy, R. C., Kaufman, Y. J., Tanré, D., Mattoo, S., Martins, J. V., Ichoku, C., Koren, I., Yu, H., and Holben, B. N.: Global aerosol climatology from the MODIS satellite sensors, *J. Geophys. Res.*, 113, <https://doi.org/10.1029/2007JD009661>, 2008.
- Remer, L. A., Levy, R. C., Mattoo, S., Tanré, D., Gupta, P., Shi, Y., Sawyer, V., Munchak, L. A., Zhou, Y., Kim, M., Ichoku, C., Patadia, F., Li, R.-R., Gassó, S., Kleidman, R. G., and Holben, B. N.: The Dark Target Algorithm for Observing the Global 775 Aerosol System: Past, Present, and Future, *Remote Sens.*, 12, <https://doi.org/10.3390/rs12182900>, 2020.
- Sawyer, V., Levy, R. C., Mattoo, S., Cureton, G., Shi, Y., and Remer, L. A.: Continuing the MODIS Dark Target Aerosol Time Series with VIIRS, *Remote Sens.*, 12, <https://doi.org/10.3390/rs12020308>, 2020.
- Sulla-Menashe, D. and Friedl, M. A.: User guide to collection 6 MODIS land cover (MCD12Q1 and MCD12C1) product., USGS Reston, VA, USA, 1, 1–18, 2018.
- 780 Yu, H., Remer, L. A., Kahn, R. A., Chin, M., and Zhang, Y.: Satellite perspective of aerosol intercontinental transport: From qualitative tracking to quantitative characterization, *Atmos. Res.*, 124, <https://doi.org/10.1016/j.atmosres.2012.12.013>, 2013.
- Vermote, E. F., El Saleous, N., Justice, C. O., Kaufman, Y. J., Privette, J. L., Remer, L., Roger, J. C., and Tanré, D.: Atmospheric correction of visible to middle-infrared EOS-MODIS data over land surfaces: Background, operational algorithm and validation, *J. Geophys. Res. Atmos.*, 102, <https://doi.org/10.1029/97JD00201>, 1997.
- 785 Zhang, H., Kondragunta, S., Laszlo, I., and Zhou, M.: Improving GOES Advanced Baseline Imager (ABI) aerosol optical depth (AOD) retrievals using an empirical bias correction algorithm, *Atmos. Meas. Tech.*, 13, <https://doi.org/10.5194/amt-13-5955-2020>, 2020.



790

Table 1 Summary of new surface reflectance parameterization for DT-GEO algorithm. Multiple linear regression, which consists of three parameters, SZA, NDVI_{SWIR}, and % land type, predicts regression slope and y-intercept between Red and SWIR surface reflectance. The listed value refers the regression coefficient and the number in parentheses indicates 1-sigma of the coefficients.

Closed Vegetation	SZA	NDVI _{SWIR}	% land type	Const
Slope (1- σ)	0.0015 (0.0006)	0.0181 (0.0540)	-0.0013 (0.0003)	0.4439
Y-int (1- σ)	-0.0002 (0.0001)	-0.0125 (0.0062)	0.0000 (0.0000)	0.0172
Open Vegetation	SZA	NDVI _{SWIR}	% land type	Const
Slope (1- σ)	0.0014 (0.0005)	-0.4477 (0.0563)	0.0001 (0.0003)	0.6729
Y-int (1- σ)	-0.0003 (0.0001)	0.0411 (0.0084)	-0.0001 (0.0003)	-0.0041
Urban	SZA	NDVI _{SWIR}	% land type	Const
Slope (1- σ)	0.0013 (0.0006)	-0.3890 (0.0620)	0.0018 (0.0005)	0.5976
Y-int (1- σ)	-0.0003 (0.0001)	0.0369 (0.0091)	-0.0001 (0.0001)	0.0024



795 **Figure 1** (a) Full disk coverage of ABIE with VZA ($< 72^\circ$) for each pixel and (b, c) MODIS VZAs for the same region on two consecutive days (Sep 01-02, 2019). The red circle indicates the location of GSFC AERONET site [$-76.84^\circ\text{E}, 38.99^\circ\text{N}$].

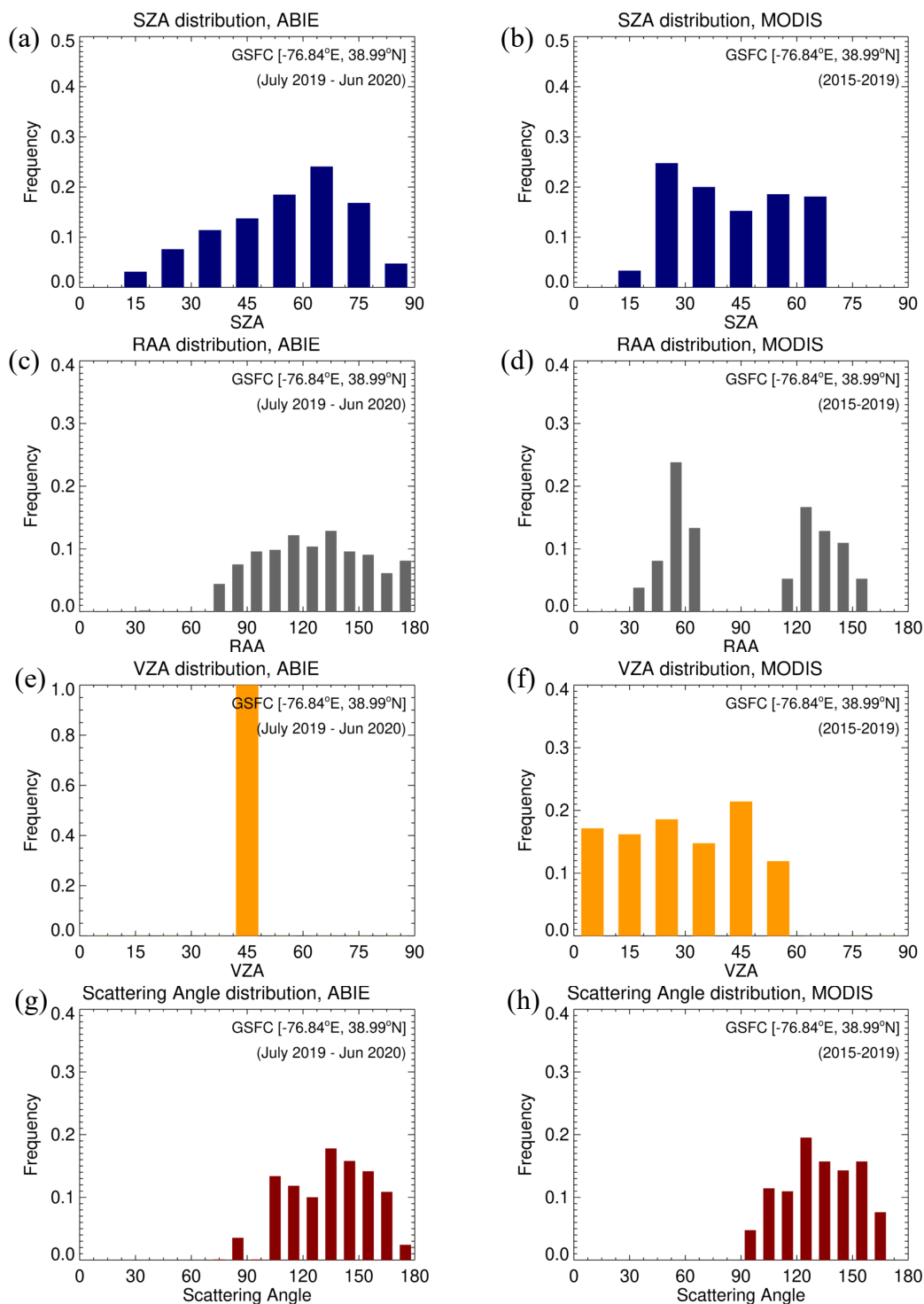
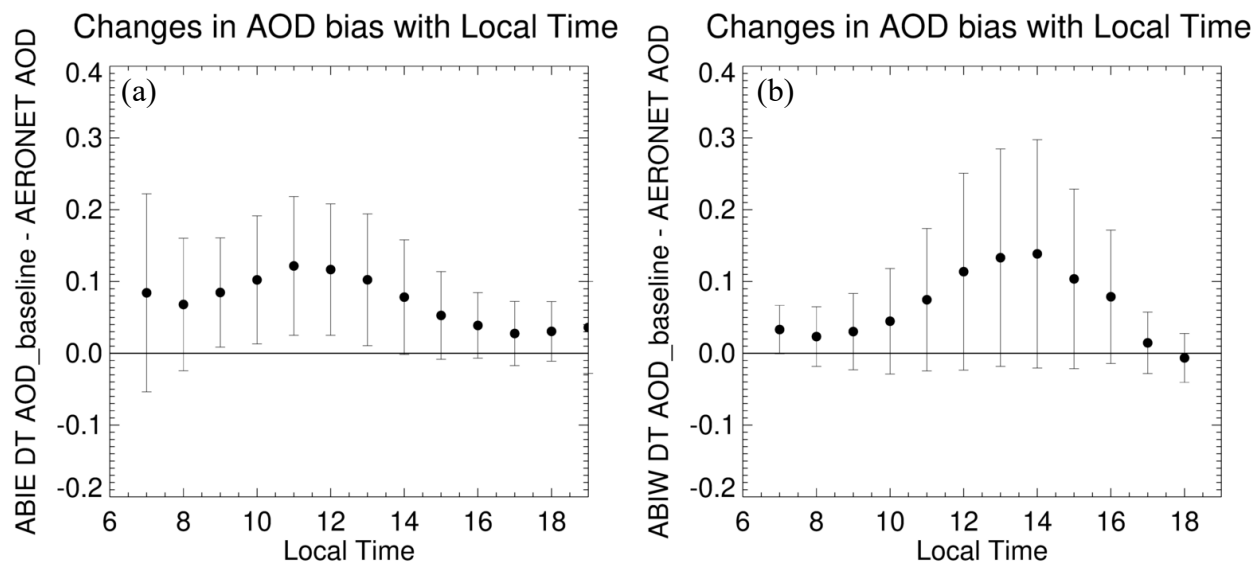
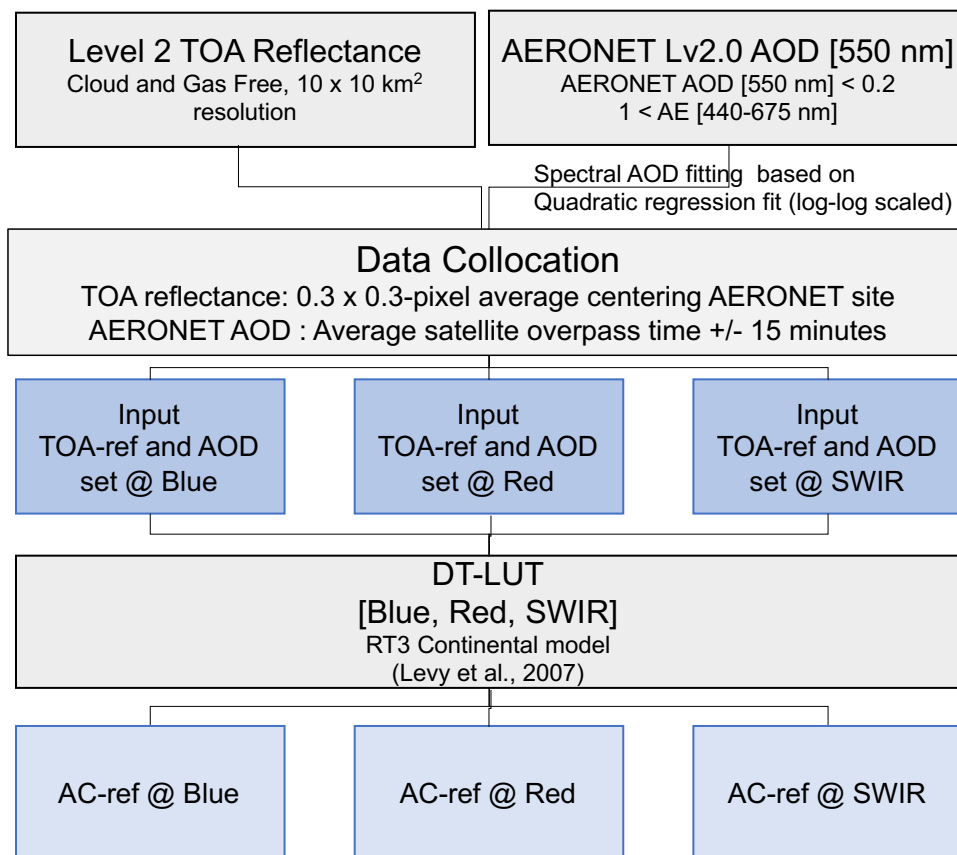


Figure 2 Frequency distributions of sun-and-sensor geometries for (left) ABIE and (right) MODIS measurements at GSFC AERONET site: (a, b) SZA, (c, d) RAA, (e, f) VZA, and (g, h) scattering angle.



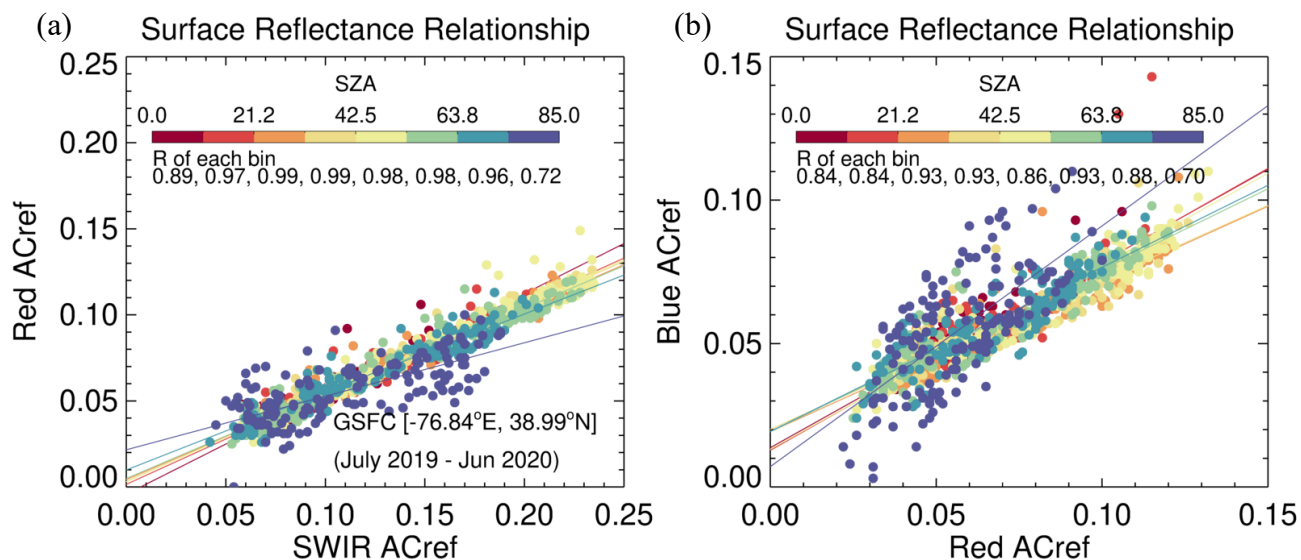
800

Figure 3 Average bias of the DT AOD against collocated AERONET values retrieved from (a) GOES 16 ABI (ABIE) and (b) GEOS 17 ABI (ABIW) from August to September 2019. The AOD biases are calculated from all available AERONET site and then averaged for each local solar time. The vertical bars represent 1-sigma range of the AOD bias at each time.

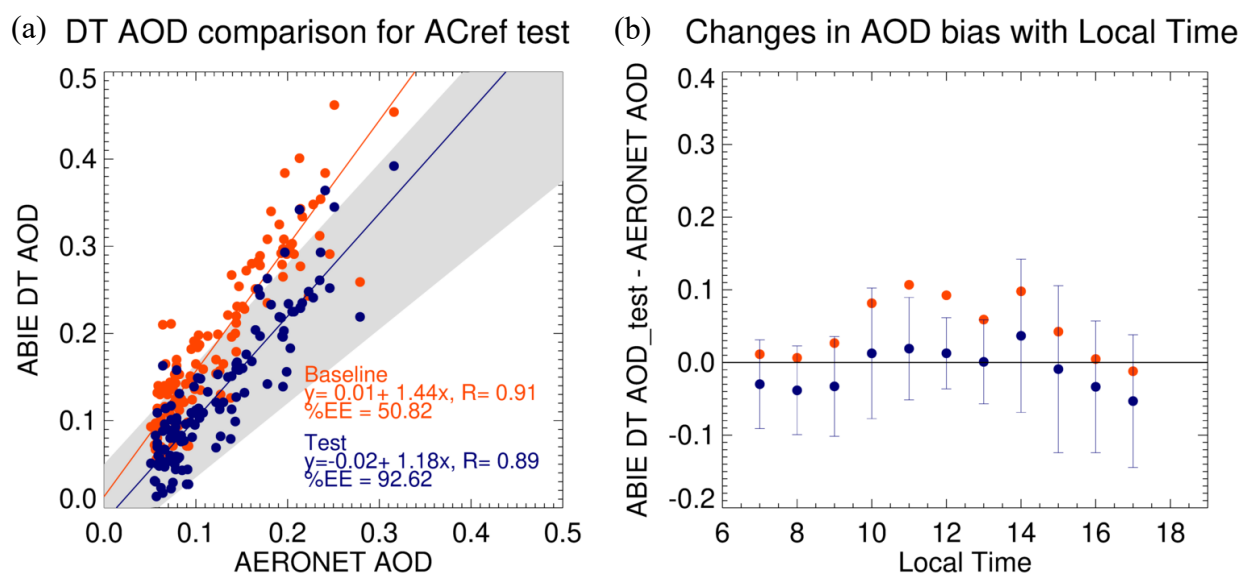


805

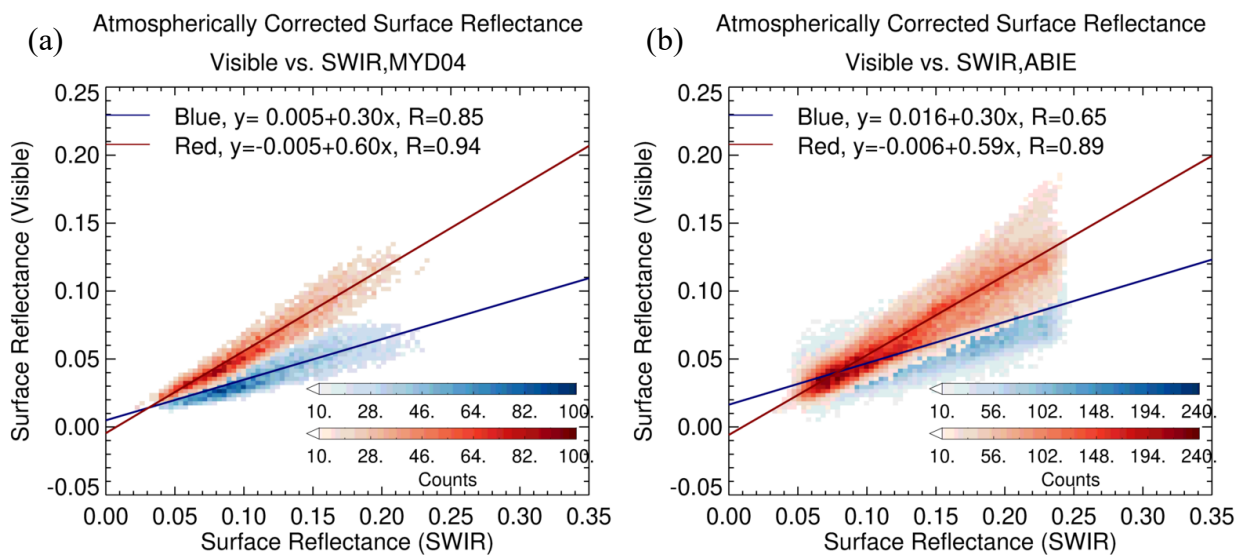
Figure 4 Flowchart of calculating atmospherically-corrected reflectance (AC-ref). The DT-LUT was created using the RT3 code, assuming a black Lambertian surface.



810 **Figure 5** Relationships between (a) Red and SWIR AC-ref and (b) Blue and Red AC-ref obtained from the GSFC AERONET site from July 2019 to June 2020. Color represents SZA and solid lines show linear regression for eight SZA groups. Each group has equal data points (144).



815 **Figure 6** Validation of DT AOD retrieved from ABIE at GSFC in September 2019; (a) Scatter plots between ABIE AOD and AERONET AOD and (b) diurnal changes in the bias between them. Orange and black indicate different assumption in surface reflectance parameterization (SRP); Orange represents the DT AOD retrieved assuming the baseline DT SRPs but blue represents the tested AOD adopting the SRPs obtained from the AC-ref of ABIE (Fig. 5).



820

Figure 7 AC-ref in the visible (0.47 and 0.66 μm for MODIS and 0.47 and 0.63 μm for ABIE) compared with SWIR AC-ref (2.12 μm for MODIS and 2.24 μm for ABIE). The (a) MODIS AC-ref consists of 5 years of observations from 2015 to 2019 over the ABIE Field of View while the (b) ABIE AC-ref is for one year from July 2019 to June 2020. Blue and red indicate Red-SWIR and Blue-SWIR relationship, respectively.

825

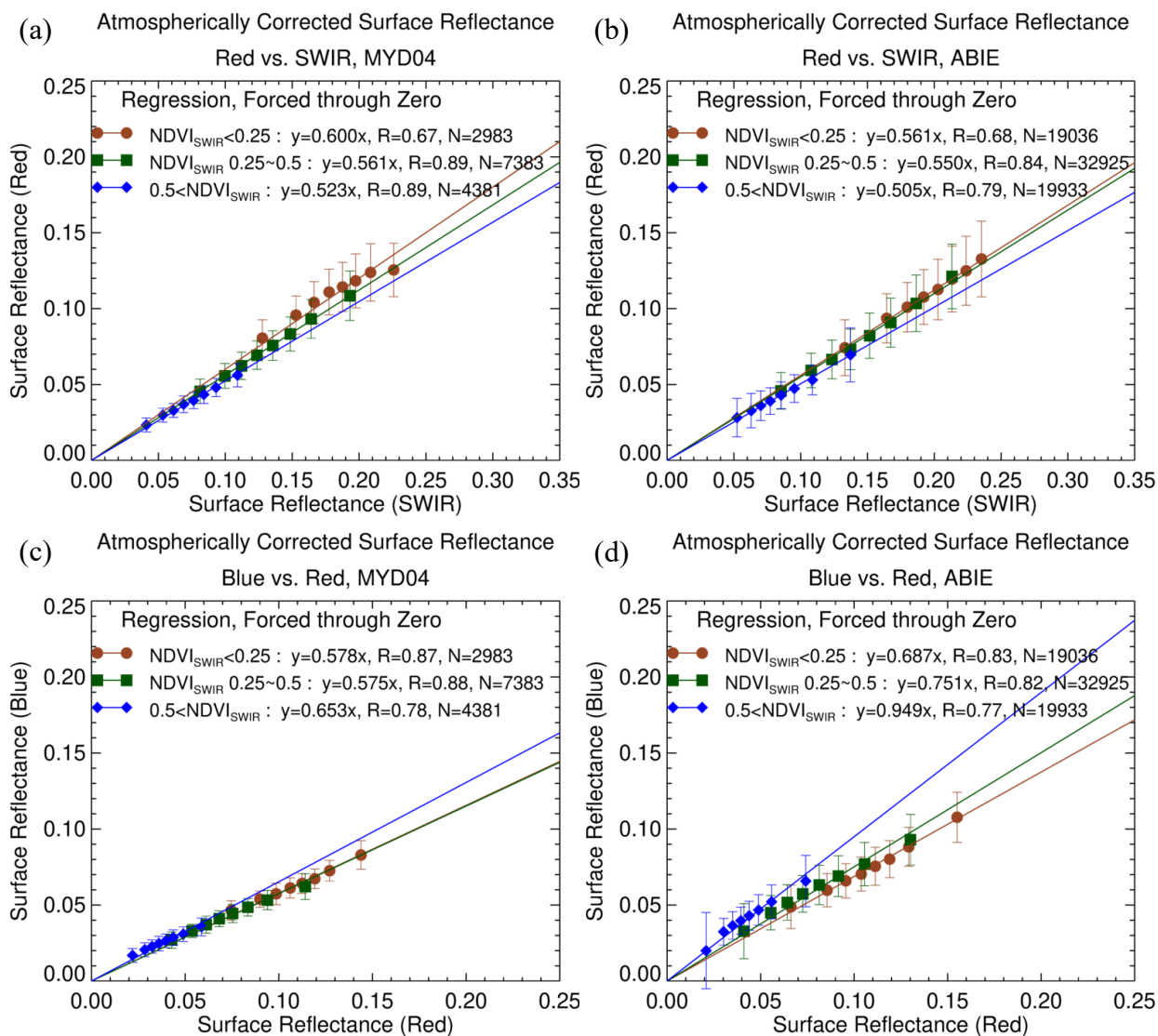


Figure 8 The AC-ref relationships (a, b) between red and SWIR and (c, d) between blue and red channel as a function of $NDVI_{SWIR}$. Left and Right columns indicate the relationships for MODIS and ABIE, respectively. The regression equation is forced through zero. Red refers to low $NDVI_{SWIR}$, green to medium and blue to high values. Each AC-ref group for $NDVI_{SWIR}$ is divided equally into 8 bins and is displayed by mean (symbol) and standard deviation (vertical bar) of each bin.

830

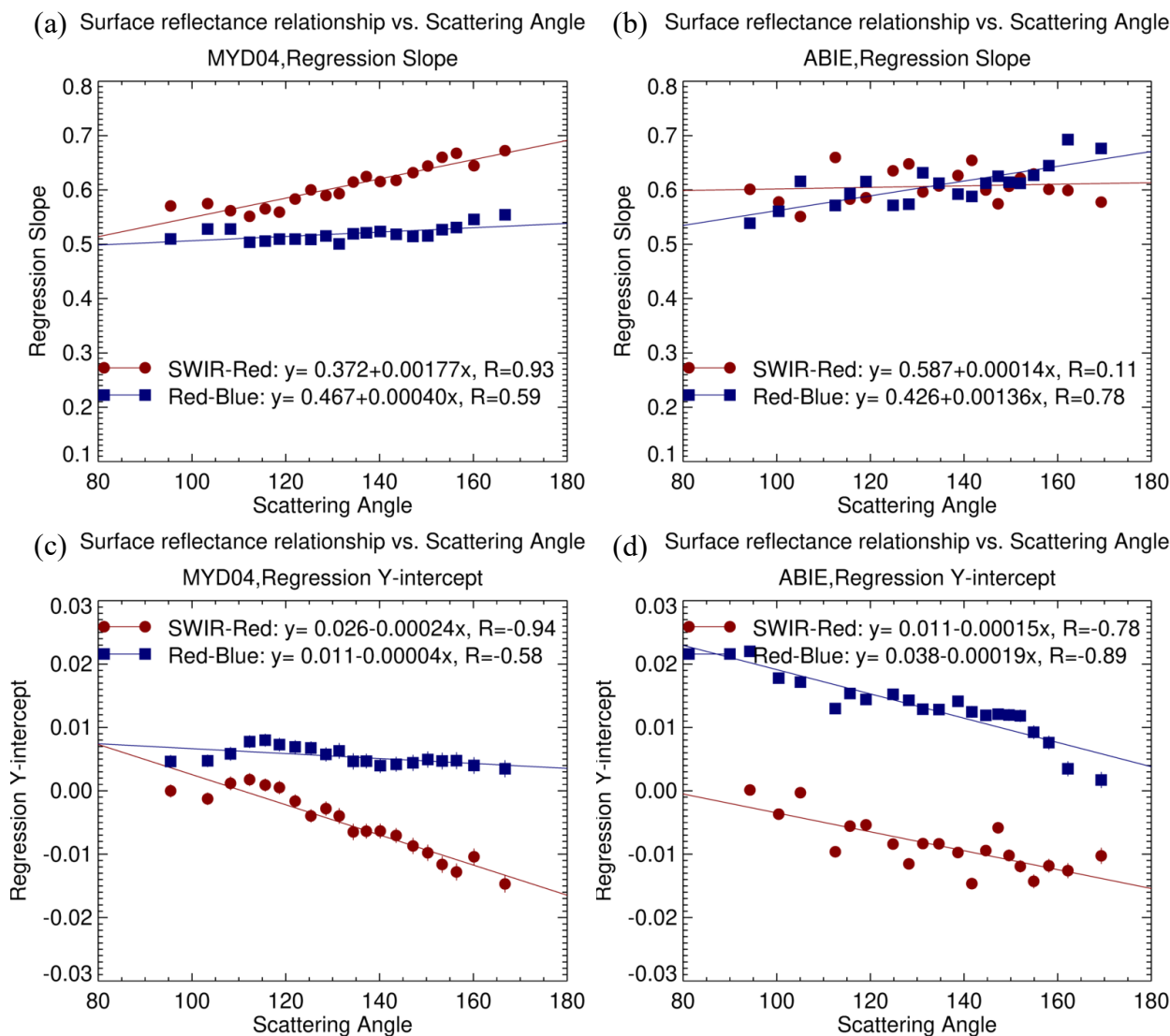


Figure 9 Regression between visible and SWIR AC-ref of (left) MODIS and (right) ABIE. Slope (a, b) and y-intercept (c, d) of regression are plotted as a function of scattering angle. The data were sorted according to scattering angle and put into 20 groups of equal size (736 for MODIS and 3899 for ABIE). Blue square and red circle indicate red-SWIR and blue-red ratio, respectively.

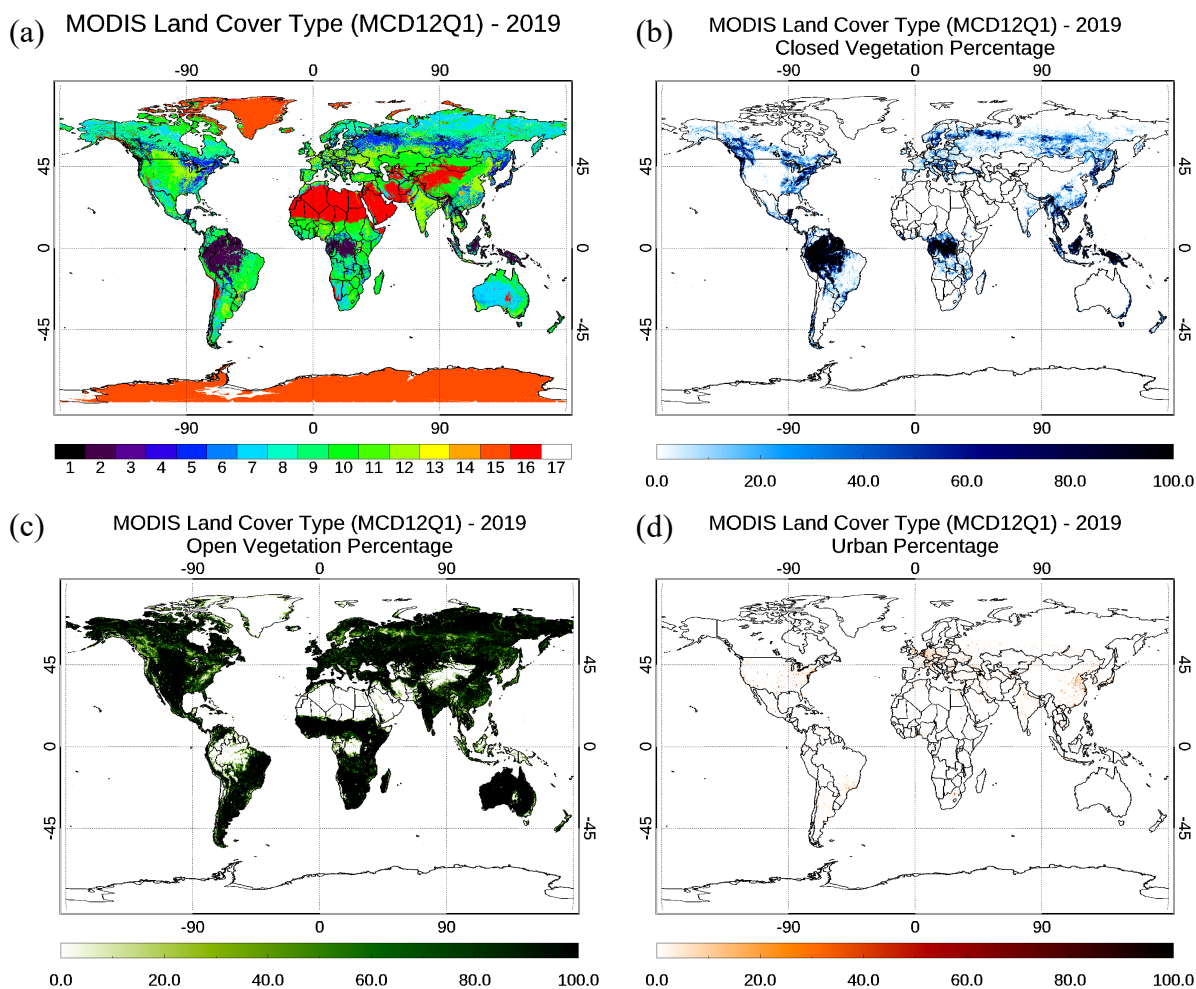
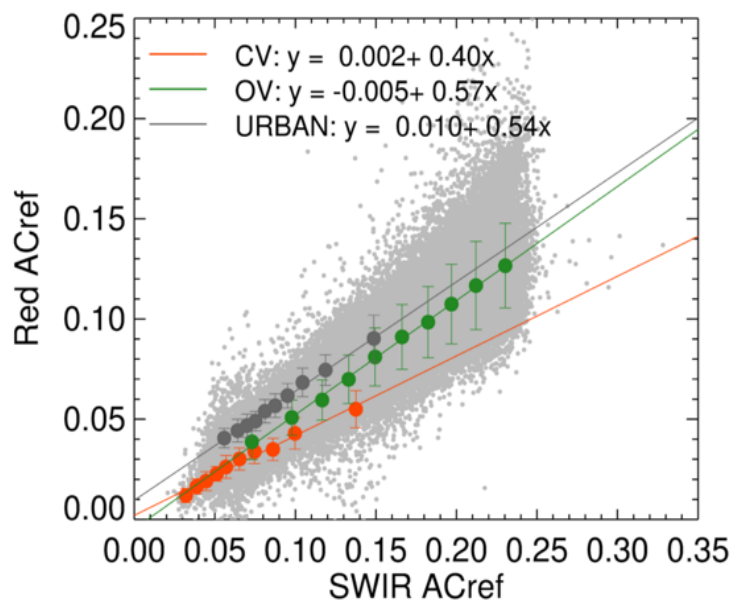


Figure 10 A global map of (a) the most frequent International Geosphere Biosphere Program (IGBP) index within $0.1 \times 0.1^\circ$ grid box and the percentage of the sub-grid index classified into (b) Closed Vegetation, (c) Open Vegetation, and (d) Urban type. The IGBP index indicates 1. Evergreen Needleleaf Forests, 2. Evergreen Broadleaf Forests, 3. Deciduous Needleleaf Forests, 4. Deciduous Broadleaf Forests, 5. Mixed Forests, 6. Closed Shrublands, 7. Open Shrublands, 8. Woody Savannas, 9. Savannas, 10. Grasslands, 11. Permanent Wetlands, 12. Croplands, 13. Urban and Built-up Lands, 14. Cropland/Natural Vegetation Mosaics, 15. Permanent Snow and Ice, 16. Barren, 17. Water Bodies.

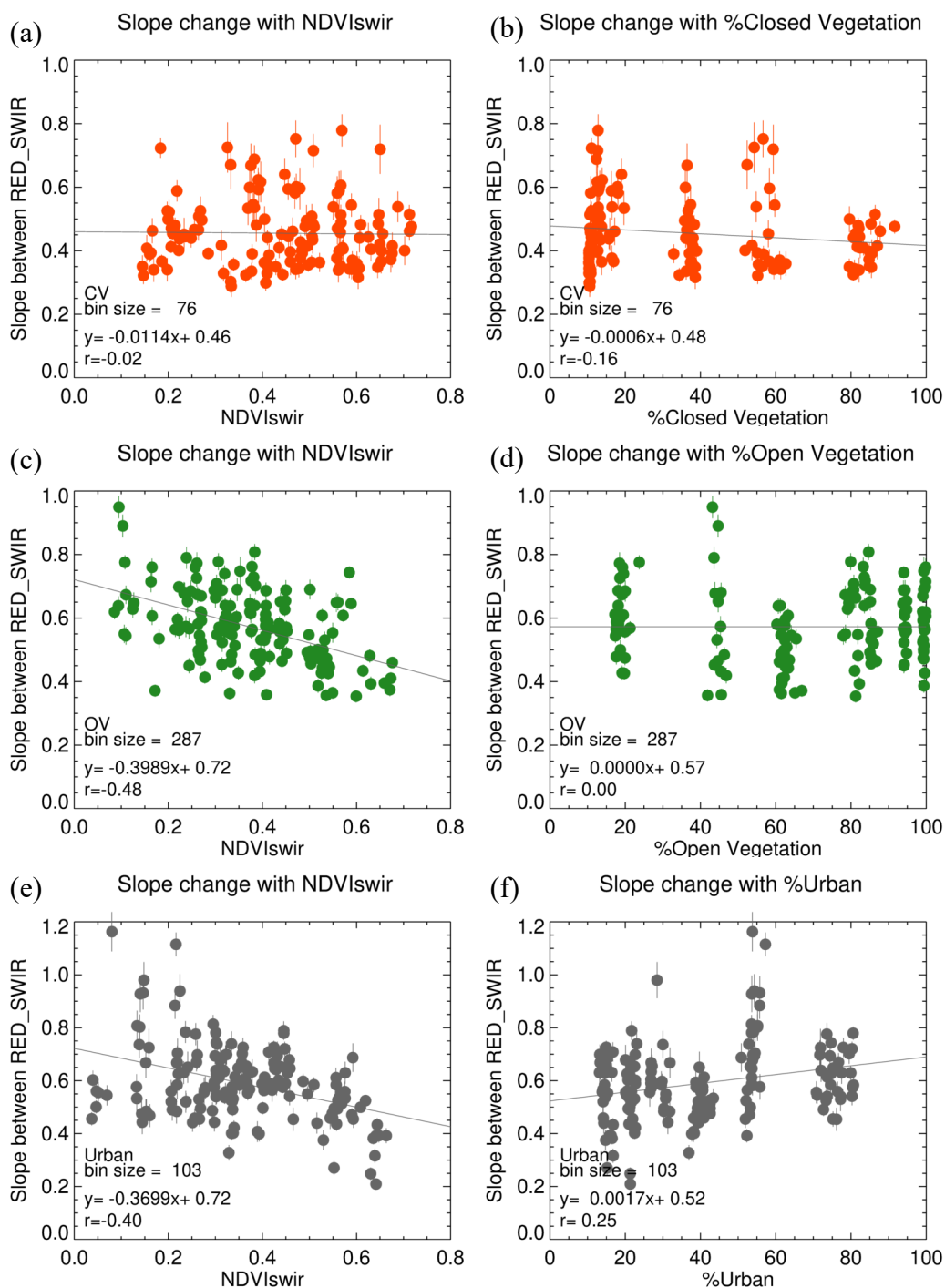
840



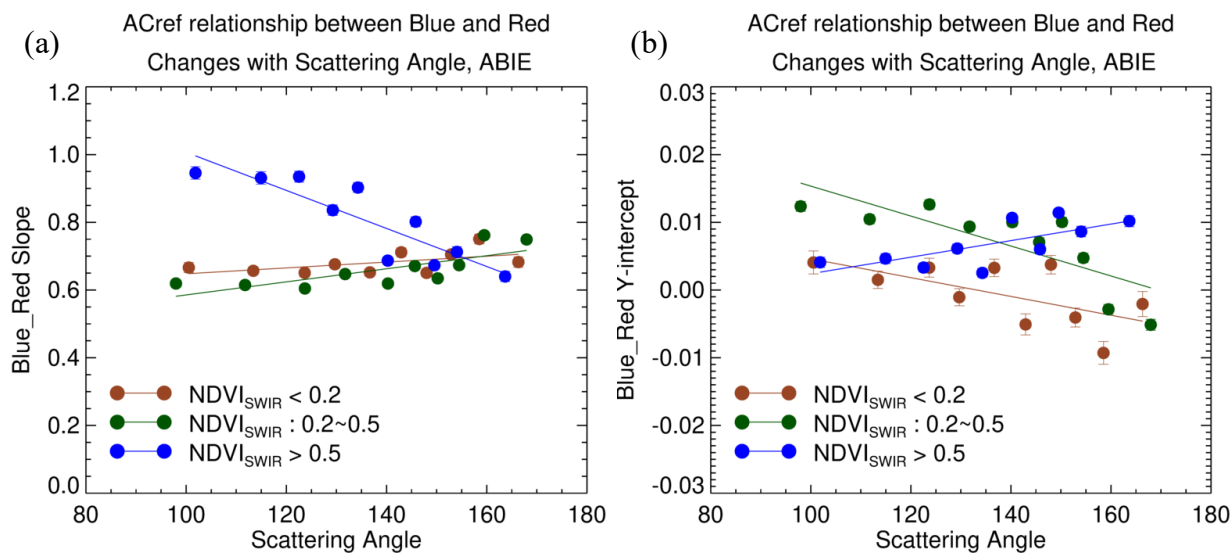
ACref relationship between ABIE Red vs. SWIR



845 **Figure 11** Linear regressions (a) between Red and SWIR AC-ref classified into three land cover types: Closed Vegetation (CV, Red), Open Vegetation (OV, Green) and Urban (Black). Each AC-ref group is divided equally into 10 bins and is displayed by mean (symbol) and standard deviation (vertical bar) of each bin. The gray dot represents a population of ACref, which is not distinguished by land type.



850 **Figure 12** Change of regression slopes in the Red and SWIR AC-ref regression according to (left) $NDVI_{SWIR}$ and (right) land type percentage. For each land type group of (a, b) Closed Vegetation (CV), (c, d) Open Vegetation (OV), and (e, f) Urban, AC-ref are equally divided into 216 bins according to SZA, $NDVI_{SWIR}$, and % land type. Vertical bar represents 1-sigma of slope. Among the 193 AERONET sites used for the collocation, 40 sites corresponded to CV, 169 sites to OV, and 55 sites to urban.



855 **Figure 13** The change of blue and red relationship with $NDVI_{SWIR}$ and scattering angle. Color indicates $NDVI_{SWIR}$ which is divided into three levels.

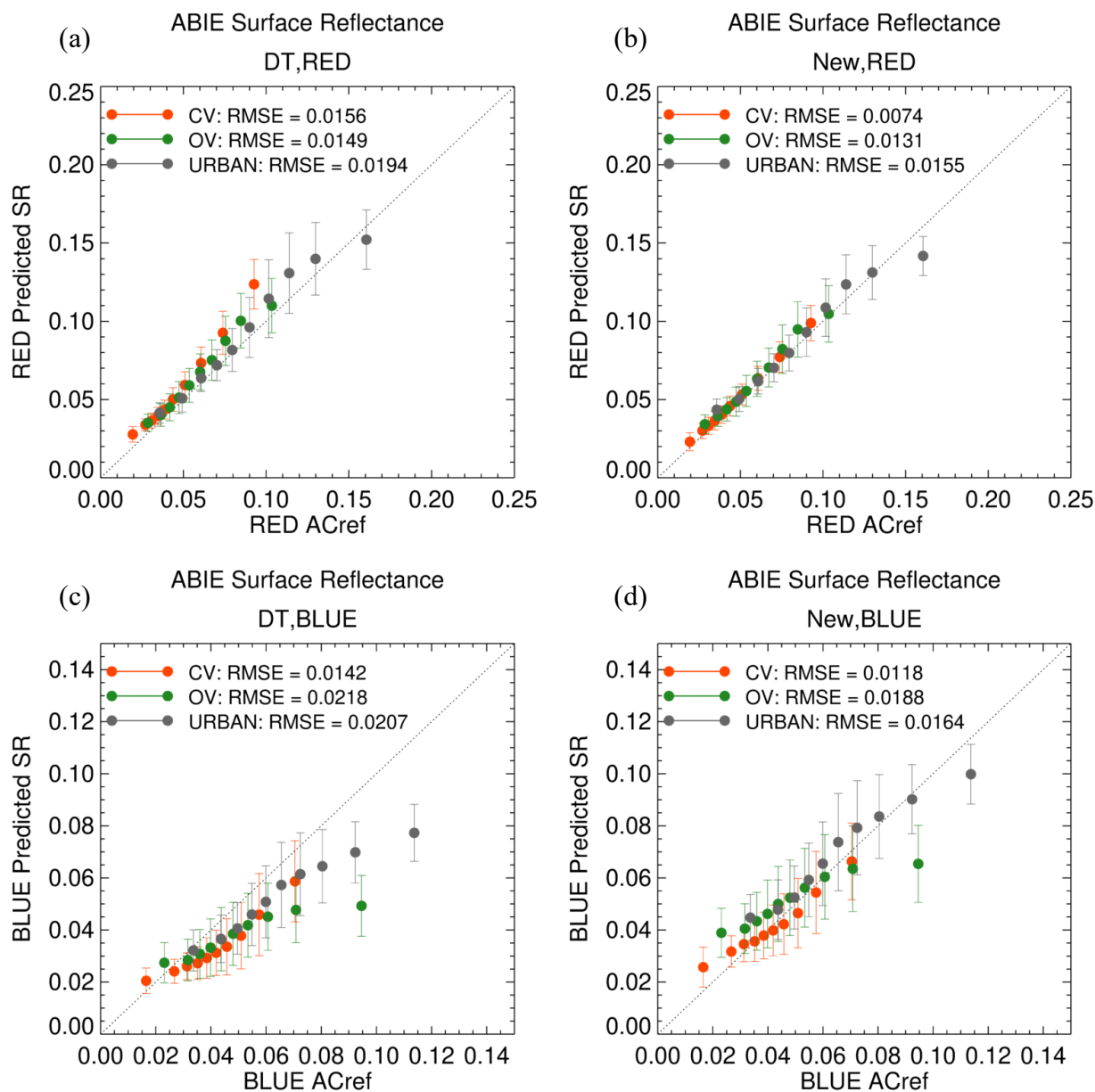


Figure 14 Comparisons between predicted surface reflectance and AC-ref for the (top) red and (bottom) blue channels. Left panels show the predicted surface reflectance achieved from the baseline DT SRP and the Right panels show the predicted surface reflectance using the new DT-GEO SRP. The predicted surface reflectance is sorted by AC-ref and equally divided into 10 bins. Symbol and vertical bar represent mean and standard deviation in each bin respectively, and color indicates land type: (red) CV, (green) OV, and (gray) Urban.

860

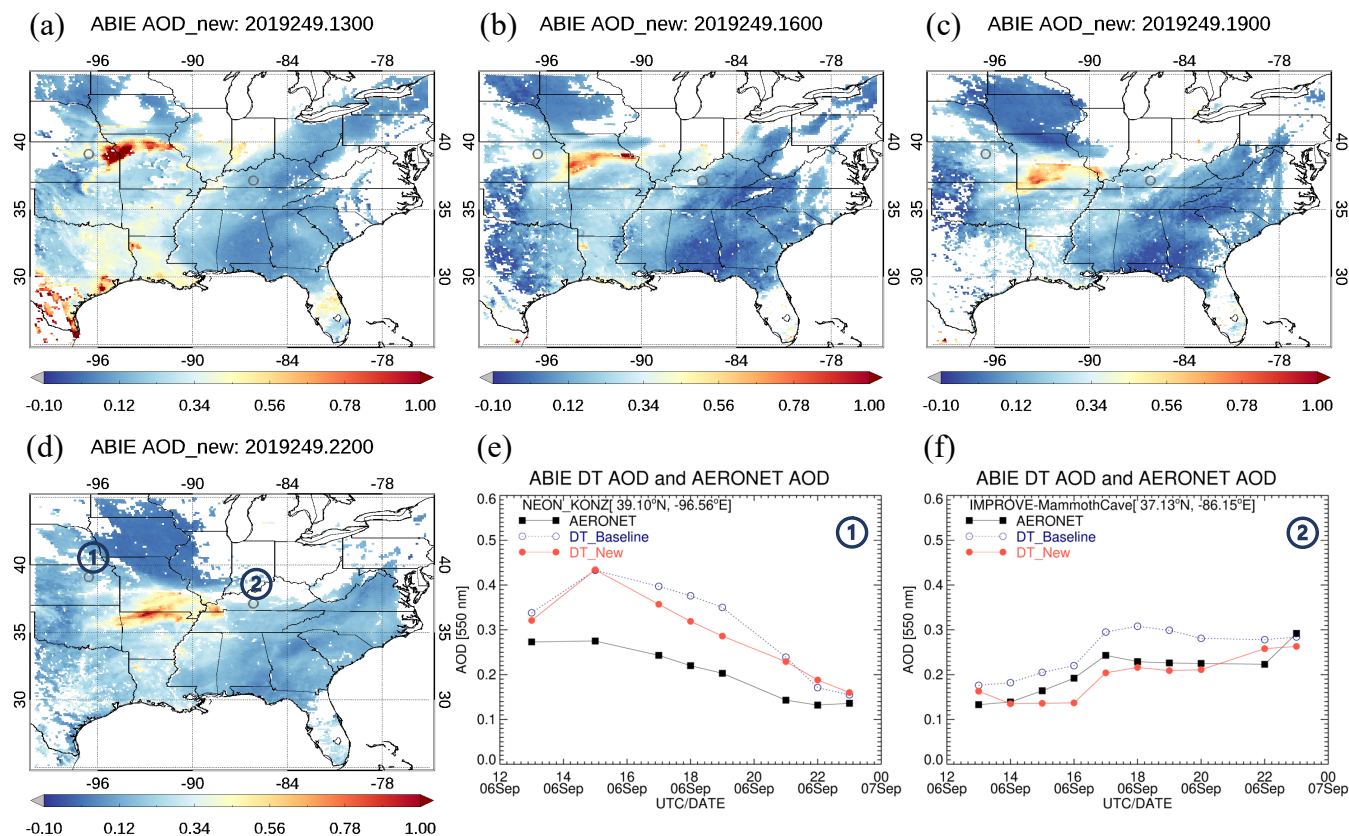
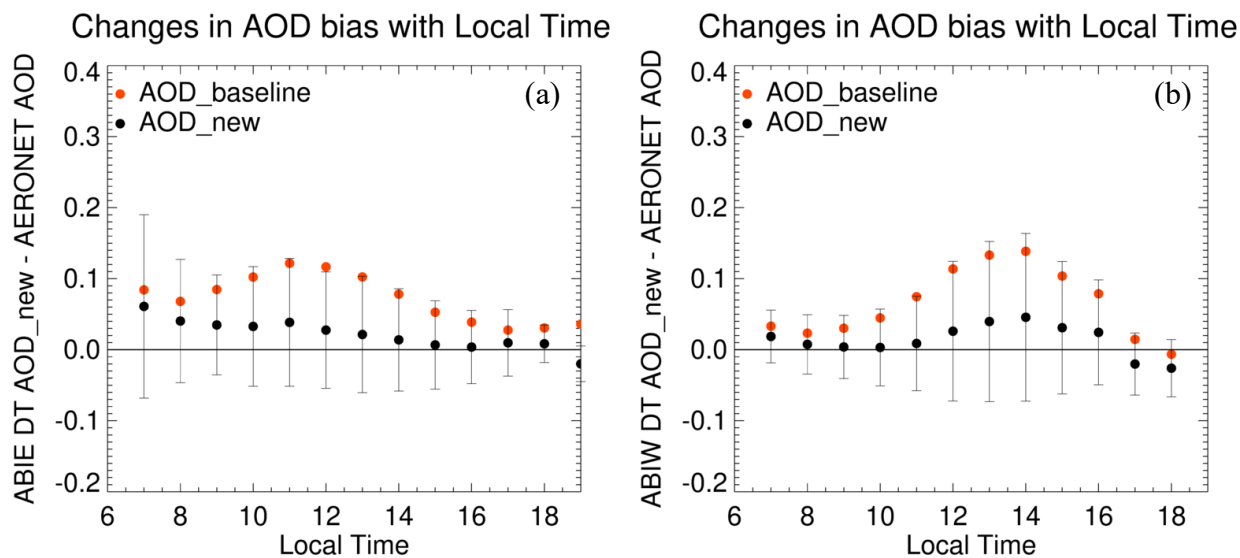
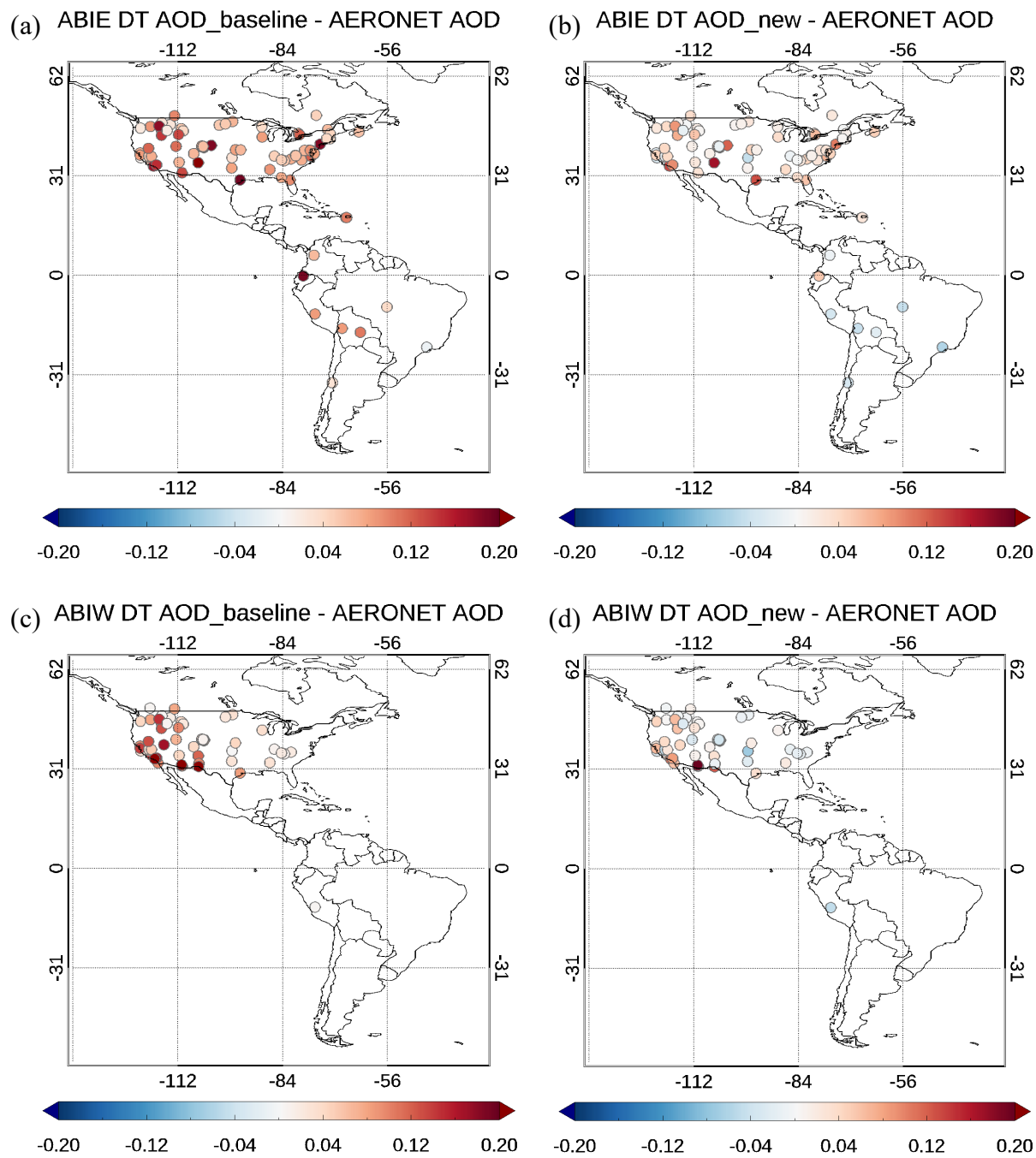


Figure 15 Three-hour interval map (a-d) displaying the new DT AOD retrieved from ABIE on September 6, 2019. A comparison is made between the new DT AOD and the baseline DT AOD as well as the AERONET AOD at two locations: (e) NEON_KONZ [39.10°N, -96.56°E] and (f) IMPROVE_MammothCave [37.13°N, -86.15°E]. A Black square indicates AERONET AOD [550 nm], a blue open circle represents the baseline DT AOD [550 nm], and a red closed circle denotes the new DT AOD [550 nm]. The AERONET sites are marked on the map with gray circle.

865



870 **Figure 16** Comparison of the bias in the DT AOD retrieved by assuming the baseline and the new surface reflectance parameterization (SRP). Average biases (Black) in the new DT AOD retrieved from (a) ABIE and (b) ABIW are overlaid on the (Red) original DT AOD bias. The vertical bars represent 1-sigma range of the new AOD bias at each time. The DT AOD obtained from August to September 2019 across all collocated AERONET stations within the sensors' disk scan.



875 **Figure 17** Bias maps of (a, c) the baseline DT AOD and (b, d) the new DT AOD retrieved from (a, b) ABIE and (c, d) ABIW for August - September 2019. The bias represents the average of the absolute difference between DT AOD and AERONET AOD.